DEVELOPMENT OF A FLUORESCENCE LIFETIME BASED METHOD TO DETECT AND ANALYZE SINGLE MOLECULE REACTIONS IN SOLUTION

BY

RYAN ANTHONY COLYER

B.S., Allegheny College, 2002
M.S., University of Illinois at Urbana-Champaign, 2004

DISSERTATION

Submitted in partial fulfillment of the requirements
for the degree of Doctor of Philosophy in Physics
in the Graduate College of the
University of Illinois at Urbana-Champaign, 2008

Urbana, Illinois

Doctoral Committee:

Professor Robert Clegg, Chair
Professor Enrico Gratton, Advisor
Professor John Stack
Professor Brian DeMarco

Abstract

Transitions between protein conformations have been found to be essential to the biological function of many proteins. These conformational transitions can be observed by the effects of Förster Resonance Energy Transfer (FRET) on fluorescence emission. We present a new fluorescence lifetime analysis method called phasor trajectory analysis (PTA) which can be used to observe these conformational transitions under single molecule conditions and on the millisecond timescale. To maximize the precision obtained from the small number of photons available for this analysis, we developed a mathematical model for digital frequency domain lifetime acquisition, which was then used to derive the hardware parameters affecting precision. Using this information, we developed a new lifetime acquisition system which makes optimal use of the photons emitted by the sample, and provides two fully independent lifetime channels.

This new hardware was used to observe the conformational dynamics of a calmodulin sample labeled with a FRET pair, and encapsulated within 100nm lipid vesicles. A toolbox of analysis techniques was developed for PTA, and was used to quantitatively describe the transitions and fluctuations of the conformation of calmodulin. Analysis was done in a model-free manner, and also by applying known parameters about the system to extract more specific information. Using the information obtained, a conformational model was developed to describe the dynamic behavior of calmodulin's conformation in terms of its binding with calcium. In addition, measurements conducted in the presence of a peptide derived from Ca^{2+}/calmodulin-dependent protein kinase II were used to examine the properties of calmodulin's conformational dynamics while interacting with its binding targets.

To my loving wife, Claudia

Acknowledgements

In a necessarily incomplete and insufficient list, I would like to acknowledge...

...My advisor Enrico Gratton for his guidance and ideas, and for exposure to a wide variety of experiences.

...My wife Claudia Lee for her constant support over the years, for an unquantifiable number of suggestions, and for working side-by-side with me on the FLIMBox.

...Jay Unruh for working with me on the calmodulin project, for refreshing my knowledge of laboratory chemistry, and for being an excellent friend.

...Christian Hellriegel for numerous interesting discussions, and for many entertaining games of chess.

...Jason Sutin for introducing me to the practical side of optics.

...Courtney Santos for adding a touch of family to work.

...All the other members of the LFD.

...My parents for 28 years of unconditional support.

...Professor Robert Cupper for inspiring me to pursue a Ph.D.

...Nobuhiro Takamizawa, Shinji Motomura, and Olympus for collaboration on the integration of the FLIMBox with their microscope.

...E. Shane Price and Carey Johnson for preparing and donating the labeled calmodulin sample.

...M. Neal Waxham for donating the CaMKII-derived peptide, and for discussions about data interpretation.

...John Wiley & Sons for permission to include the portions of Chapter 2 which were previously published and are ©2008 John Wiley & Sons, Inc.

...And the NIH for funding, as part of PHS 5 P41 RR03155.

Table of Contents

List of Figures

List of Tables

List of Abbreviations

AFD	Analog Frequency Domain
APD	Avalanche Photodiode
CaM	Calmodulin
CaMKII	Ca^{2+}/Calmodulin Dependent Protein Kinase II
cps	counts per second
DFD	Digital Frequency Domain
EF	Oedema Factor
FCS	Fluorescence Correlation Spectroscopy
FLIM	Fluorescence Lifetime Imaging Microscopy
FPGA	Field Programmable Gate Array
FRET	Förster Resonance Energy Transfer
HMM	Hidden Markov Model
MLE	Maximum Likelihood Estimation
PMT	Photomultiplier Tube
PTA	Phasor Trajectory Analysis
RFH	Rise-Fall Histogram
RICS	Raster Image Correlation Spectroscopy

TAC	Time-to-Amplitude Converter
TCSPC	Time-Correlated Single Photon Counting
TDC	Time-to-Digital Converter

Overview of the Dissertation

The main goal of this thesis was the development of a new method for the analysis of single molecule reactions in solution using fluorescence lifetime. This work began in 2005 with the goal of developing a low-cost multi-channel photon counting lifetime imaging card which acquired lifetime information in the form of phasors and could accumulate counts at a high burst rate without saturation. As technical and theoretical work continued on this project, a complete theoretical description of the acquisition method and its uncertainty was developed, which led to the optimization of the lifetime precision to a level close to the theoretical maximum. Chapter 2 of this thesis focuses on the development of this hardware, the theoretical description of its operation, and the derivation of these phasor uncertainty relations.

While examining the implications of the phasor uncertainty relations, we realized that our optimized acquisition hardware yielded a precision level adequate for the observation of lifetime changes of a single fluorophore on a millisecond timescale. Chapter 3 of this thesis describes the phasor trajectory analysis which extends existing phasor techniques to the observation of dynamic changes in lifetime as with FRET efficiency changes, presents a method for merging donor and acceptor lifetime information, and extends the phasor uncertainty relations to this analysis approach.

In Chapter 4, the optimized two-channel acquisition card developed in Chapter 2, the analysis approach presented in Chapter 3, and the detailed uncertainty analysis were applied to the study of physiologically relevant single molecule reactions of calmodulin. This new approach created a significant volume of data showing the direct conformational fluctuations of calmodulin in the presence of various binding partners. Several new analysis methods are presented in Chapter 4 which enabled a detailed analysis of the conformational basis for the reactions observed, and which yielded quantitative values describing the dynamic molecular interactions with calmodulin's binding partners.

Chapter 1

Introduction

1.1 Overview

As instrumentation and analysis techniques advance, there has been a substantial increase in the number of single molecule studies. Single molecule techniques have great appeal for researchers because they allow direct and detailed examination of the molecular interactions behind processes. For studying biological systems, fluorescence lifetime based single molecule techniques offer unique advantages because they allow measurements to be made in a fairly non-invasive manner, and provide a high rejection of background interference. However, the number of fluorescence lifetime based single molecule studies has been significantly constrained by the expense of hardware and the difficulty of analysis. In this thesis we present hardware advancements and new analysis techniques which make fluorescence lifetime based single molecule techniques practical and straightforward. We also present a detailed study with calmodulin which demonstrates the capability of this new approach to address physiologically relevant questions.

In this chapter, a historical context is presented for the work, along with the theoretical background which led to the developments presented here.

1.2 Single Molecule Reactions

Single molecule studies using fluorescence have found a wide variety of applications since they allow the study of molecular and conformational states and fluctuations, and interactions with individual binding partners. In this way, behaviors can be studied directly which would be eliminated or made difficult to observe with an ensemble measurement. Single molecule experiments are able to distinguish subpopulations by analyzing each molecule one at a time and categorizing the molecules based on an observable property. A single molecule measurement can also track the dynamic changes of a single molecule as a function of time. This capability is the focus of Chapter 4, where dynamic changes in conformation were used to study the interactions of a molecule with its binding partners.

1.2.1 Studies of Biological Systems

Two major applications of single molecule techniques to the study of biological systems have been the measurement of distances between points on DNA, and the measurement of conformational states of proteins [13, 30]. Both of these applications use Förster Resonance Energy Transfer (FRET) to observe nanometer scale changes in distance between labeled parts of a macromolecule.

Studies have used fluorescence lifetime based FRET measurements to accumulate histograms of FRET states, and have used intensity based FRET to observe transitions between protein conformations [30]. However, the field is lacking a method for fluorescence lifetime based observation of FRET transitions which can operate with the low counts obtainable under single molecule conditions, on a millisecond timescale, and in the presence of a significant background.

The approach presented in this thesis uses a fluorescence lifetime based approach to observe FRET fluctuations due to protein conformational changes, and does so in a rigorous way which can function in the presence of a significant fluorescence background.

1.3 Fluorescence Lifetime

1.3.1 Background

Fluorescence lifetime is a fundamental spectroscopic quantity that allows quantitative analysis through several approaches, including the identification of molecular species based on lifetime, FRET, contrast due to different ion concentrations, and measurements of chemical equilibria.

When a fluorescent molecule is excited into its excited state, the probability distribution for when a photon is emitted becomes an exponential decay of the form $e^{-t/\tau}$, where τ is the lifetime of the fluorophore. The fluorescence lifetime of a fluorophore can be sensitive to the chemical environment or the proximity of other molecules. This property allows fluorescence lifetime to be used as a tool for performing quantitative analysis of molecular structures, chemical environments, and biological systems.

Because fluorescence lifetime is independent of the fluorescence intensity, it can be used as a measuring tool which is independent of fluorophore concentration, detection efficiency, or intensity of the illumination used for excitation. This makes fluorescence lifetime particularly valuable within microscopy, where it is used to provide intensity-independent image contrast between different molecular species, ion concentrations, or relative distances between paired fluorophores with FRET.

1.3.2 Burst Integrated Fluorescence Lifetime

Recently a technique known as Burst Integrated Fluorescence Lifetime (BIFL) has been developed and utilized for the analysis of the lifetimes of single molecules as they pass through the focal volume of a microscope. Most BIFL experiments are analyzed using an exponential fitting approach to determine the lifetime, which requires all or most of the photons within a burst to determine a lifetime value for that burst, and which utilizes both expensive pulsed lasers and expensive acquisition hardware [17]. After a large number of bursts are integrated, the BIFL approach allows a histogram to be constructed which shows the distribution of lifetimes for the molecule being observed. However, the distributions shown in these histograms do not allow the observation of transitions or fluctuations of FRET within a single molecule.

1.3.3 Statistical Modeling

Since there is value in observing transitions between different FRET states, two statistical modeling methods called Maximum Likelihood Estimation (MLE) and Hidden Markov Modeling (HMM) have been developed which allow the observation of these transitions [16, 32, 39]. These methods utilize a probabilistic analysis to extract the most likely underlying state sequence given a time sequence of photons from a single-molecule burst.

With HMM, the system is modeled as a set of states with probabilities of transitions between those states, and then the most likely sequence of states is determined. The results obtained from this analysis depend upon knowing the probabilities of transitions between each state. The probabilities of the transitions must either be known initially, or must be determined by an iterative fitting process, and incorrect values in the transition matrix can result in changes to the sequence of states which results from the HMM analysis.

When used to examine millisecond timescale FRET fluctuations, an intensity based MLE method has been shown to have results similar to the binning of photons into time bins, followed by using Equation 1.1 [39]. This is a reasonable expectation for intensity sequences analyzed with any of the statistical modeling approaches, since they are ultimately using the same information, which is the relative intensity between two channels. This means that an intensity based statistical modeling analysis is subject to the same underlying problems with background and inhomogeneity that are described in Section 1.4 for intensity-based FRET.

The use of MLE to observe dynamic changes of lifetime values can yield some of the advantages of a lifetime based approach, but this typically requires around 150 photons per time bin of interest [17]. Also, MLE analysis can become complicated in the presence of model uncertainty, such as in the presence of background contributions. In an environment with significant background, MLE analysis could result in bias which is difficult to predict, and it would be difficult to analytically estimate the uncertainty of the resulting values.

1.4 Förster Resonance Energy Transfer

Förster Resonance Energy Transfer (FRET) is a dipole-dipole interaction which results in a nonradiative transfer of energy from the excited state of a donor molecule to an acceptor molecule [19]. This dipole-dipole interaction can only occur if the fluorescence emission spectrum of the donor overlaps with the absorption spectrum of the acceptor, and it usually has an operating distance between around 1 to 10 nanometers [11]. Because of this scale of operation, FRET is sometimes referred to as a "molecular ruler" in that it can allow one to use fluorescence to monitor the distance between a donor and an acceptor which are both attached to a single molecule.

The efficiency of energy transfer, called the FRET efficiency, is defined as [11, 19, 39]:

$$E = \frac{cI_A}{cI_A + I_D} = 1 - \frac{\tau_{DA}}{\tau_D} = \frac{1}{1 + \left(\frac{R}{R_0}\right)^6} \tag{1.1}$$

where I_D and I_A are the intensity of the donor and acceptor emission, and where τ_{DA} and τ_D are the lifetime of the donor in the presence of the acceptor, and the lifetime of the donor without the acceptor present. This can then be related to the distance R between the donor and the acceptor using the rightmost term where R_0 is the Förster radius for that FRET construct.

This relationship provides two different methods of determining the FRET efficiency, the first being the intensity-ratio method, and the second being the lifetime method. In an ideal world they would yield the same result, however the two methods are subject to different types and sources of error. The intensity-ratio method is evaluated by the relative intensities in two collection channels after a calibration, c, which corrects for the spectral range of each channel. Because it is based on intensity, this approach to FRET has greater problems with acceptor quenching and inhomogeneities in intensity or in the background. Since diffusing particles naturally experience changes in intensity as they move through the focal volume, these problems can manifest in single-molecule studies of dynamic behavior as systematic error.

Lifetime based approaches to FRET allow the FRET efficiency to be determined in one or both channels in a manner that is independent of the relative intensities of the two channels, and in a manner which does not depend significantly on the spectral range of the filters. Traditionally, lifetime based FRET has not been used for millisecond timescale FRET fluctuations because fitting to an exponential curve requires more photons than are typically available in the desired timescale. We will show in Chapter 3 that a phasor trajectory analysis provides sufficient precision that it becomes possible to use the robustness of a lifetime based approach to FRET for the observation of these fluctuations on the millisecond timescale.

1.5 Fluorescence Lifetime Acquisition

1.5.1 Time-Correlated Single Photon Counting

Time-Correlated Single Photon Counting (TCSPC) is a fluorescence lifetime acquisition technique which measures the lifetime of a sample by determining the arrival time of each photon with respect to the laser pulse. This is usually done with a picosecond scale precision for the determination of each photon's arrival time, which is accomplished by using an expensive time-to-amplitude converter (TAC) or time-to-digital converter (TDC). This approach achieves a high level of precision, but with the expense of the converters limiting the ability to scale to multiple parallel channels. In addition, the converters are the limiting factor in detection count rate, restricting the maximum burst count rate to about 8 million counts per second, and with dead times after each photon count of around 125ns.

Data acquired with TCSPC systems is commonly analyzed by fitting the data to a sum of exponentials, each one representing a single lifetime component. In biological systems this can become a significant difficulty because individual fluorophores can have multiple exponentials, multiple fluorophores can be present in a region of interest, and cells frequently exhibit background counts in the form of autofluorescence which itself contributes multiple exponentials. In a microscopy environment with a biological sample, there are typically only enough total counts to fit a few exponentials at best [36].

Similar difficulties appear with single molecule studies. Under single molecule conditions, there are very few counts available, and with a small number of counts it is not guaranteed that a fit to even a single exponential will converge properly. Accumulating a larger number of counts would require more time, which raises the lower limit of the timescale which can be observed. Attempting to perform a single molecule lifetime analysis within a cellular environment in the presence of a multi-exponential background by fitting to multiple exponentials would require the accumulation of such a large number of counts that this would prohibit the observation of fast dynamics.

1.5.2 Analog Frequency Domain

The Analog Frequency Domain (AFD) lifetime approach for confocal microscopy is typically done by heterodyning, or modulating the photomultiplier tube (PMT) at a frequency slightly offset from the frequency at which the laser is modulated, f_{ex}. The difference between these two frequencies is then the cross-correlated beat frequency of the output, which is slow enough to be detected by inexpensive electronics. The lifetime values are then represented by the phase shift, ϕ_F, and modulation, m_F, of this cross-correlated signal. These values are transformed into the lifetime values τ_p and τ_m by [42]:

$$\tau_{p,h} = \frac{1}{2\pi h f_{ex}} \tan\left(\phi_{F,h}\right) \tag{1.2}$$

$$\tau_{m,h} = \frac{1}{2\pi h f_{ex}} \sqrt{\frac{1}{m_{F,h}^2} - 1} \tag{1.3}$$

1.6 Phasor Analysis

Phasor analysis is a frequency domain analysis method for fluorescence lifetimes which provides a number of intrinsic advantages. With the phasor approach, lifetimes can be analyzed without fitting the emission response to an exponential decay. Also, when lifetimes are treated as phasors, multiple lifetimes add linearly, and the instrument response can be easily accounted for by vector operations [24]. While phasor analysis is a frequency domain analysis method, it is not limited to the analysis of only data acquired by frequency domain hardware. Any data which has a time sequence with lifetime information can be analyzed by phasor analysis using a Fourier transform. This makes phasor analysis a general approach which can be applied to lifetime data acquired by any system.

This approach is growing rapidly as a tool for lifetime images due to its ability to obtain quantitative results with no fitting, and the ability to present changes in FRET efficiency or relative fluorophore concentration in a visually straightforward manner [9, 37, 14]. In this thesis, phasor analysis is also shown to have an analytically calculable precision, and to scale well to low count conditions [12]. These techniques are then extended to a Phasor Trajectory Analysis (PTA) which permits the observation of fluorescence lifetime dynamics under single-molecule conditions.

Chapter 2

Digital Frequency Domain Lifetime Acquisition*

2.1 Overview

This chapter presents a new theory for digital frequency domain (DFD) lifetime acquisition, a detailed analysis of the precision obtained from any system when phasor analysis is used, and a hardware implementation of the DFD algorithm. The hardware implementation was developed by designing a new digital circuit which was implemented on a Field Programmable Gate Array, yielding a two-channel lifetime imaging acquisition device which was easily duplicated at low expense. The DFD theory and the phasor uncertainty analysis presented here were used to optimize the parameters of the hardware so that the precision was near the theoretical maximum.

2.2 Introduction

We have developed a physical implementation and statistical model of a new method for lifetime data collection and analysis. Our approach falls in the category of the "frequency domain" approach to lifetime acquisition, yet uses a detector operating in the photon counting mode. This digital frequency domain (DFD) method overcomes the problems of duty cycle, modulation of the detector gain, and expensive radiofrequency synthesizers used in the classical analog frequency domain approach.

---

* Portions of this chapter have been published in [12], are ©2008 John Wiley & Sons, Inc., and are reprinted with permission.

In our approach we implemented all the operations performed in a frequency-domain lifetime instrument in a digital form using a single field programmable chip. Since all operations including the generation of the light modulation frequency, the generation of the cross-correlation sampling frequency and the assignment of the time of arrival of a photon to a bin are digital, there are no calibrations or adjustments to be performed. The mathematical model presented below fully accounts for all the elements of the DFD method. In addition, the mathematical model reproduces, as a limiting case, the principle of the TCSPC approach. Therefore, on a common statistical basis we can compare the two approaches and derive some general conclusions about the relative precision of the two methods. We found that with proper system design the two methods can be made to have comparable precision. More importantly, the mathematical model was used to maximize the precision of the DFD implementation and to determine which parameters are crucial to reach optimal performance. In terms of precision of the lifetime measurement, we were able to fully quantify the effect of the instrument response including the jitter of the detection system.

2.3 Existing Measurement Techniques

For measurements done in a cuvette, in which spatial resolution is not needed, there are two major approaches to the acquisition of the fluorescence decay. One is based on TCSPC or time-sampling of the intensity decay after pulse excitation, and a second is based on the measurement of the harmonic response of the fluorescence system.

When spatial resolution is needed, such as with microscopy, different considerations come into play depending on the kind of microscope used. One major difference between laser scanning confocal microscopes and camera based microscopes is that in the former the detector works in the serial mode, although there are some recent scanning instruments using multiple foci in conjunction with a camera to collect the image [21, 44]. For lifetime instrumentation operating in the serial mode, a bottleneck in the rate of data acquisition is caused by the recovery time of the TAC element that is common to the TCSPC based instruments.

During the last few years, several new instruments were introduced for lifetime measurement in the confocal microscope by several manufacturers. As a consequence, fluorescence lifetime imaging microscopy (FLIM) has become more common and is now available in several labs. One of the reasons for the interest in FLIM is that FRET imaging by lifetime resolved methods is generally considered to have fewer problems with background and autofluorescence than intensity ratio methods. However, FLIM methods are limited to few labs due to the high cost of the instrumentation and the difficulty of performing lifetime analysis in many pixels simultaneously [36]. The analog frequency-domain approach offers some simplification in the analysis methods and in the laser sources used [10]. However, the traditional frequency-domain electronics operating in the radio frequency range require gain modulated detectors, radio frequency amplifiers [22], and are not a simple addition to existing laser confocal microscopes. Whatever approach is utilized, current methods are relatively expensive, require specialized electronic and modulated sources, and involve sophisticated analysis methods to extract information about the lifetime image and the processes that produce lifetime variations in different pixels of an image [36].

2.4 A New Digital Approach

We present new data acquisition hardware that requires minimal modifications to the configuration of common commercial laser confocal microscopes. The cost of the new electronics is minimal. We also use the phasor method of data analysis that is "native" to the proposed hardware and simplifies the calculation and presentation of lifetime images. Overall, the proposed approach has the potential to make FLIM technology more widely available. Our approach uses serial detectors in the photon counting mode, and the digital heterodyning method to acquire data which is directly analyzed in the frequency domain. The principle of the digital heterodyning method was described as part of a previous thesis [18]. However, the original implementation by Eid et al. used a specialized acquisition card and had limitations in terms of the duty cycle and speed of data acquisition. In Section 2.8 we develop a mathematical model of DFD-FLIM (Digital Frequency Domain FLIM). Using this model we were able to choose optimal system parameters which minimize the distribution of lifetime values, as described in Section 2.9. Using an FPGA chip, we have implemented a version of the digital heterodyning method which has a 100% duty cycle so that no photons are lost, operates in several harmonic frequencies simultaneously, can be used in conjunction with common detectors in commercial laser scanning microscopes, only requires a modulated light source instead of a pulsed source, has uncertainty levels comparable to TCSPC methods, and has very high throughput with a very low cost. The cost of the FPGA chip and evaluation board is below $100. The mathematical model contains, as a limiting case, the description of data acquisition using the TCSPC method of data acquisition. Using the model, we were able to compare theoretically and experimentally the proposed DFD and the TCSPC methods, and to conclude that they have the same statistical accuracy. We were also able to predict the effect of instrument jitter on the precision of the DFD approach and to conclude that there is an optimal jitter level that improves the precision of the determination of very short lifetimes.

We implemented the DFD approach in several confocal microscopes, both with 1-photon and 2-photon excitation, and with home built and commercial instruments. As shown below, the hardware collects data directly under the form of "phasors" at several harmonic frequencies simultaneously. The phasor representation of the fluorescence decay allows a very simple interpretation of the FLIM image and the calculation of FRET efficiencies without the usual translation of the decay into exponential components. The phasor approach to data analysis for both solution and image measurements has been previously described [9, 24, 4, 37]. It provides a simple graphical interface for FLIM data presentation and analysis without the need for fitting the fluorescence decay at each pixel. We compared data collected with the DFD and TCSPC methods on the same sample. After optimization of the design parameters, the DFD approach gave results comparable to those obtained with TCSPC.

2.5 Digital Frequency Domain Hardware

Traditional analog approaches to frequency domain acquisition use modulation of the gain of a PMT or of an image intensifier. For digital frequency domain lifetime acquisition, we replace the modulation of these analog signals with a digital modulation scheme inside the data collection circuitry (rather than at the detector level) by using multiple sampling windows within each excitation period, as shown in Figure 2.1. Because the modulation is performed digitally, the signal can be processed by an arbitrary number of sampling windows without any loss of signal, and the PMT can be operated at full gain during the entire acquisition.

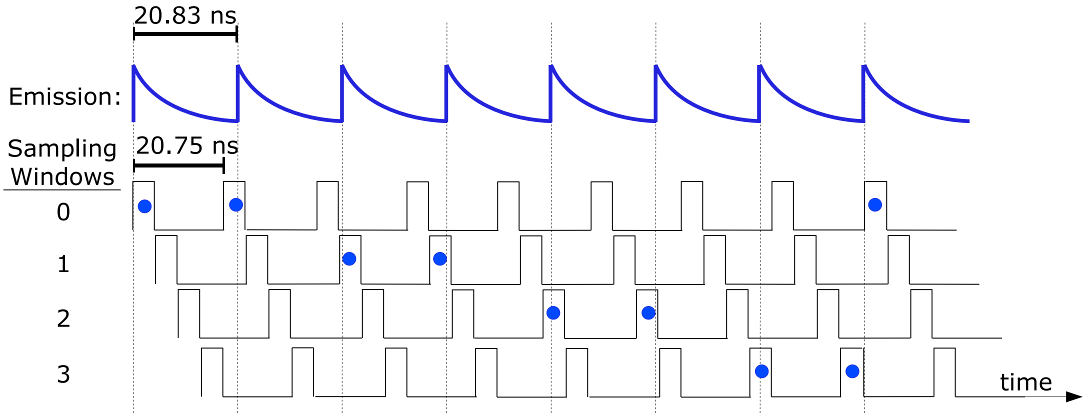

Figure 2.1: An illustration of the digital heterodyning principle, with exaggerated heterodyning such that $f_{cc} = f_s/8$ instead of $f_{cc} = f_s/256$ which we used in our implementation. Arriving photons (dots) are assigned to one of four sampling windows according to their arrival time. In the real case, the sampling windows slide through the entire period of the emission response due to the slight difference in frequencies after a total of 256 steps.

To achieve sensitivity to short lifetimes and to ensure evenly distributed sampling of the fluorescence emission, we use heterodyning between the frequency of the sampling windows and the excitation frequency of the light source, as shown in Figure 2.1. As will be described below, this allows us to translate the fluorescence response into a cross-correlation phase histogram, as shown in Figure 2.2, which contains a functional form given by the convolution of the fluorescence emission with the shape of the sampling window.

We created a device called the FLIMBox, in which the digital frequency domain algorithm is implemented in a system which uses a field programmable gate array (FPGA). An FPGA is a chip which can be rapidly reprogrammed with different circuit layouts by uploading firmware, and thus serves as a convenient tool for the development of scientific hardware. The specific FPGA we used was a Xilinx® Spartan® 3E, XC3S100E™ (San Jose, CA), on an Avnet Electronics Marketing Evaluation Kit (Phoenix, AZ) with a Cypress EZ-USB FX2™ chip (San Jose, CA).

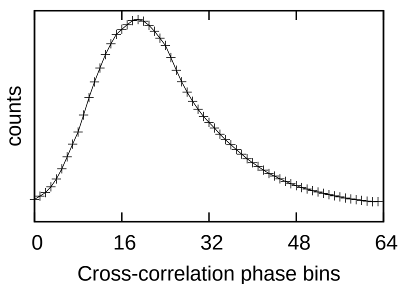

Figure 2.2: A histogram of counts received at each phase value of the cross-correlation period. Plots such as this one contain the exponential decay of a fluorophore, convolved by the instrument response function.

The FPGA contains two digital clock managers (DCMs) which provide clock synchronization to an external clock and clock multiplication services. Each DCM multiplies an input clock frequency by n_d/m_d, where n_d and m_d are integers ranging from 1 to 32. To implement the heterodyning principle in a digital system, it is convenient to have a cross-correlation frequency which is a whole integer fraction of the sampling frequency, f_s. To reach the minimal uncertainty plateau described in Section 2.9, at least four sampling windows are required. This can be obtained by choosing $n_1 = 32$, $m_1 = 17$, $n_2 = 32$, $m_2 = 15$, and dividing the frequency by four, such that a clock is generated which is four times the sampling clock. The resulting sampling frequency and cross-correlation frequency of $f_{cc} = f_s/256$, are given by:

$$
\begin{aligned}
f_s =& \frac{n_1 n_2}{4 m_1 m_2} f_{ex} && (2.1)\\
f_{cc} =& \left| \frac{n_1 n_2}{4 m_1 m_2} - 1 \right| f_{ex} && (2.2)
\end{aligned}
$$

For example, for a 48MHz excitation frequency, a 4X clock is generated at 192.8MHz, yielding a sampling frequency of 48.188MHz and a cross-correlation frequency (the difference between the light modulation and the sampling frequency) of 188kHz. This fast 4X clock is then used as the input for a counter which tags incoming photons with the sampling window number (0 to 3) which corresponds to their arrival time.

To relate the window during which a photon arrived to a portion of the excitation period, it is necessary to know the relative phase difference between the sampling and excitation clocks. For digital stability of this phase difference measurement, this was implemented as a cross-correlation phase counter which counts at the time scale of the sampling clock, has a periodicity equal to the cross-correlation frequency, and uses negative feedback on the measurement of the excitation clock to lock on to a consistent phase relationship. This circuit enforces the same phase relationship between the cross-correlation counter and the sampling and excitation clocks each time the device is activated. Therefore the cross-correlation phase counter provides a consistent measurement of the relative phase difference between the sampling and excitation clocks during each sampling period.

The circuit then outputs a value identifying the arrival window, w_{arr}, and the cross-correlation counter value, p_{ccc}, for each photon count. For our implementation, these two values can be combined to form a cross-correlation phase bin number as follows:

$$
p = 255 - \left[\left(p_{ccc} + \frac{256 w_{arr}}{n_w} \right) \mathrm{mod} 256 \right] \qquad (2.3)
$$

where n_w is the total number of sampling windows. This cross-correlation phase bin number is used to construct the cross-correlation phase histogram, $H(p)$, which is a histogram of the bin numbers for all the detected photons.

A requirement for imaging in a raster-scan instrument is a mechanism for scanner synchronization, so that the system can ensure that the data for each pixel is acquired at the same physical position without significant drift. A scan enable control line was included in the chip which enables data collection only when it is active, allowing the scanner control mechanism to signal when each frame (or line) has started. We then use the total time of arrival of a photon with respect to the starting of the frame (macro-time) to divide the information into pixels, each of which has a corresponding phase histogram.

2.6 System Layout

The complete schematic layout can be seen in Figure 2.3, where an example is shown with the FLIMBox installed on a commercial confocal system with a modulated diode laser. For the data in this chapter, we used an Olympus FluoView FV1000 (Olympus America, Center Valley, PA) with a variety of modulated diode lasers from ISS (Champaign, IL). The diode laser is driven by a 48MHz LVTTL signal produced by the FLIMBox which is high for 45° of the repetition period. In other system configurations we have also used 80MHz titanium:sapphire lasers in place of a modulated diode laser.

To provide an optical phase reference, the laser output is then split by a beam splitter which deflects a portion of the light to a GHz photodiode (Det200, Thorlabs, Newton, NJ). This photodiode signal is then amplified and sent to a zero-crossing trigger which produces an LVTTL signal that goes into the FLIMBox and serves as a frequency and phase reference for f_{ex}. The main portion of the laser is sent into the microscope. Without this optical phase reference, we found that the laser

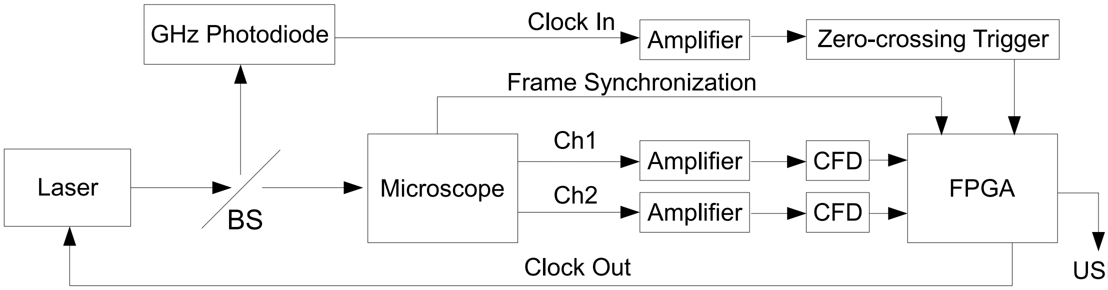

Figure 2.3: Experimental setup with the FLIMBox attached to a microscope. The microscope provides the signals from two detectors Ch1 and Ch2 and a Frame Synchronization signal. The FPGA unit is programmed by custom firmware to perform the digital frequency domain acquisition.

can sometimes introduce an unpredictable and significant phase shift which disrupts phase accuracy. With the optical phase reference in place, the system was stable to within 0.1° in phase.

The outputs of the photomultiplier tubes (PMTs) for two channels are sent to GHz amplifiers (ACA-4-35-N, Becker & Hickl, Berlin, Germany), which are then connected to constant fraction discriminators (CFDs) (Model 6915, Phillips Scientific, Mahwah, NJ) which trigger an LVTTL signal on the zero-slope of the PMT response when it goes past a set threshold.

The photon count LVTTL signals are processed inside of the FLIMBox on two fully independent channels. The photon arrival time information is then placed into a FIFO, from which the data is transferred via USB to a computer for processing.

The cross-correlation phase histogram at each pixel, $H(p)$, is then constructed by a computer program and used for the FLIM analysis.. The intensity image can be obtained by simply summing the n_p points of the phase histogram at each pixel as follows:

$$N = \sum_{p=0}^{n_p-1} H(p) \tag{2.4}$$

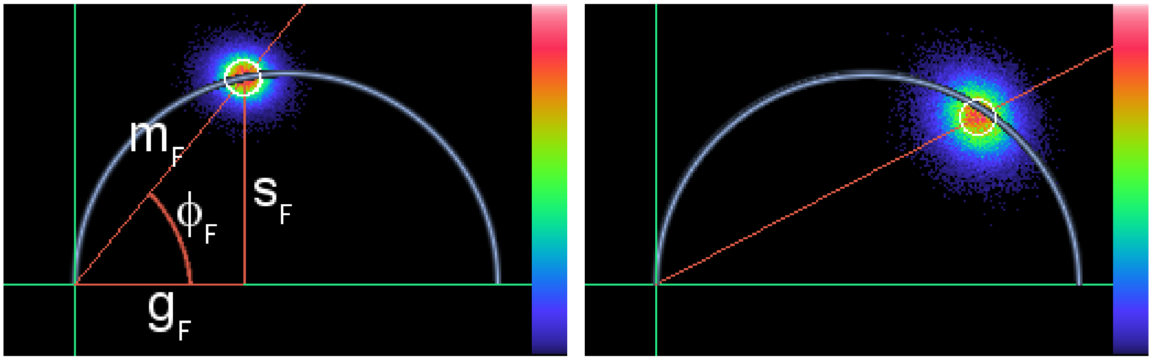

(a) fluorescein in pH 10 (538 counts/pixel) (b) rhodamine B in water (202 counts/pixel)

Figure 2.4: Normalized phasor histograms acquired at 48MHz. Only the phasor histogram for the first harmonic is shown.

2.7 Phasor Calculation

Given a phase histogram, the phasor coordinates g and s are determined for each harmonic h of the phase histogram as follows:

$$g_{H,h} = \frac{1}{N} \sum_{p=0}^{n_p-1} H(p) \cos\left(2\pi hp/n_p\right) \tag{2.5}$$

$$s_{H,h} = \frac{1}{N} \sum_{p=0}^{n_p-1} H(p) \sin\left(2\pi hp/n_p\right) \tag{2.6}$$

where N is the total number of photons and n_p is the number of bins in the phase histogram.

From these two terms, the phase and modulation values are calculated according to the vector transformation equations:

$$\phi_{H,h} = \tan^{-1}\left(\frac{s_{H,h}}{g_{H,h}}\right) \tag{2.7}$$

$$m_{H,h} = \sqrt{g_{H,h}^2 + s_{H,h}^2} \tag{2.8}$$

The g and s values are plotted as shown in Figure 2.4a, which also shows the geometric relationship with the modulation, m, and phase, ϕ.

The instrument response function is accounted for by scaling and rotation of the phasor using a reference phasor from a known reference lifetime. The modulation and phase values of the known lifetime are inserted into Equations 2.26 and 2.27 to obtain the modulation factor and phase shift of the instrument response at each harmonic of interest. This allows one to completely account for the response of the system with a single measurement.

A global representation of FLIM images at any given harmonic frequency can be obtained by turning ϕ_F and m_F back into instrument response corrected versions of the cosine and sine values of the Fourier transform.

$$g_{F,h} = m_{F,h} \cos(\phi_{F,h}) \tag{2.9}$$

$$s_{F,h} = m_{F,h} \sin(\phi_{F,h}) \tag{2.10}$$

Each pair of $g_{F,h}$ and $s_{F,h}$ values can be treated as a vector called a phasor, and these values can be accumulated on a two-dimensional histogram called a phasor plot, as shown in Figure 2.4a.

Presenting FLIM data in this format provides a number of advantages. Since the g and s coordinates come from Equations 2.5 and 2.6, they are both intensity normalized linear coordinates. The application of the instrument response only performs a scaling and a rotation, so this does not disrupt the linearity. Since g and s are linear, this means that the phasor positions of multi-exponential lifetimes are the vector sum of their single-exponential phasors. This also means that each pixel with multiple molecular species has a phasor position which is a vector sum of the phasors for each species, according to:

$$g_{F,h} = \sum_i f_{i,h} g_{i,h} \tag{2.11}$$

$$s_{F,h} = \sum_i f_{i,h} s_{i,h} \tag{2.12}$$

where $f_{i,h}$ are the fractional fluorescence intensities of each phasor component such that:

$$\sum_i f_{i,h} = 1 \tag{2.13}$$

With knowledge of the relative brightness of two species, this property of the phasors allows one to extract relative concentrations with ease. Using Equations 1.2 and 1.3 we can see that all single-exponential lifetimes occur when $\tau_p = \tau_m$, and thus when $m_{F,h} = \cos(\phi_{F,h})$ [24]. This corresponds to a semicircle on the phasor plot called the "universal circle" as shown in Figure 2.4. The functional form of this universal circle is given by:

$$\left(g - \tfrac{1}{2}\right)^2 + s^2 = \left(\tfrac{1}{2}\right)^2 \tag{2.14}$$

All multi-exponential lifetimes are therefore linear combinations of single-exponential lifetimes, as given by Equations 2.11–2.13, and therefore all multi-exponential lifetimes have phasors which are inside the universal circle.

2.8 DFD Lifetime Theory

To maximize the ability of DFD-FLIM hardware to determine lifetimes, we must reduce the uncertainty spread of phasors in the phasor plot. In Figure 2.4, where the plot is an experimental histogram of phasors at each pixel, a decrease in uncertainty would correspond to more pixels having phasors closer to the center of the phasor distribution, or a decrease in the uncertainty of the phase and modulation. To achieve this, we developed a theoretical model of the data acquisition and processing which shows which experimental parameters are important and how to change these parameters to minimize the width of the phasor distribution. Consider an arbitrary normalized fluorescence excitation function $E(t)$ modulated at a frequency f_{ex}, which can be written as a Fourier series,

$$E(t) = 1 + \sum_h 2m_{E,h} \cos\left(2\pi h f_{ex} t - \phi_{E,h}\right) \tag{2.15}$$

where $m_{E,h}$ is the modulation of the excitation at each harmonic, and $\phi_{E,h}$ is an arbitrary phase shift. The probability distribution for the fluorescence emission is given by the convolution between the excitation function and the fluorescence response of the fluorophores. For an arbitrary combination of fluorophores, the fluorescence response function can be written as:

$$F(t) = f_0 + \sum_i \left(\frac{f_i}{\tau_i \left(1 - e^{-1/(f_{ex}\tau_i)}\right)}\right) e^{-t/\tau_i} = 1 + \sum_h 2m_{F,h} \cos\left(2\pi h f_{ex} t - \phi_{F,h}\right) \tag{2.16}$$

where τ_i are the fluorescence lifetimes, f_i are the fractional intensities, and f_0 is the contribution of the uncorrelated background. This emission is then detected by a photomultiplier tube (PMT) (or other photon counting device), a discriminator, and a logic gate, with a total time response jitter which can be approximated as a Gaussian:

$$J(t) = \frac{1}{\sigma_j \sqrt{2\pi}} e^{-t^2/\left(2\sigma_j^2\right)} = 1 + \sum_h 2m_{J,h} \cos\left(2\pi h f_{ex} t - \phi_{J,h}\right) \tag{2.17}$$

where σ_j is the standard deviation of the detection time jitter, composed of a transit time spread, discriminator jitter, and triggering jitter for the digital logic. The arrival time is then resolved within the circuit into one of n_w arrival time windows, each of which is shaped as a periodic boxcar function.

$$S_{w_{arr}}(t) = \begin{cases} f_s & \text{if } \frac{w_{arr}}{n_w f_s} \leq \left(t \bmod \frac{1}{f_s}\right) < \frac{w_{arr}+1}{n_w f_s} \\ 0 & \text{otherwise} \end{cases} = 1 + \sum_h 2m_{S,h} \cos\left(2\pi h f_s t - \phi_{S,h}\right) \tag{2.18}$$

where w_{arr} is the index of the arrival time window being considered (ranging from 0 to $n_w - 1$), and f_s is the sampling frequency. Since this sampling process is performed digitally, every photon is counted in one of the sampling windows, resulting in a 100% duty cycle. We note that if the number of sampling windows is very large, this model corresponds to the data produced by the TCSPC method. However, with TCSPC the assignment of the photon to a given bin is obtained by measuring the time delay between emission and excitation with a TAC (Time-to-Amplitude Converter) or TDC (Time-to-Digital Converter). In the DFD method the assignment is done by tagging the photon with a number equal to the phase shift between the sampling and excitation clocks.

The probability distribution of the emission is naturally given by the convolution of the excitation function with the fluorescence response function. Similarly, the probability distribution for the digitized photons, prior to being sampled by the detection electronics, is given by the convolution of the preceding with the jitter of the system, giving us a probability distribution of digitized photons according to:

$$D(t) = E(t) * F(t) * J(t) \tag{2.19}$$

If the sampling of the photons with the detection electronics were done at the same frequency as the excitation, then the integral of $D(t)S_{w_{arr}}(t)$ over one sampling period would give the probability of detecting a photon within that sampling period and window. However, in Equation 2.1 we specified that in order to detect lifetime information by heterodyning, the sampling frequency was set to a different frequency than the excitation. The result of this is that the probability of detecting a photon within one sampling period is given by:

$$\int_0^{1/f_s} D(t')S_{w_{arr}}\left(t' - \frac{p}{n_p f_s}\right) dt' \tag{2.20}$$

where p is the bin number from Equation 2.3 which corresponds to the phase difference between the sampling and excitation clocks during that sampling period. This equation is equivalent to convolving $D(t)$ with $S_{w_{arr}}(-t)$ over the sampling period, and has a periodicity of n_p sampling periods, which is equivalent to the cross-correlation frequency [42]:

$$f_{cc} = |f_s - f_{ex}| \tag{2.21}$$

We can see that each of the n_w arrival time windows represented by $S_{w_{arr}}(t)$ will result in an identical probability distribution, but with a phase offset $w_{arr}/\left(n_w f_{cc}\right)$. This allows us to recombine the data acquired from the separate sampling windows during data processing into a single probability distribution $H(t)$.

Therefore, we calculate the final probability distribution of the detected photons by convolving the excitation, fluorescence response, jitter of the system, and sampling window:

$$H(t) = E(t) * F(t) * J(t) * S(-t) \tag{2.22}$$

This equation can be greatly simplified by using the convolution theorem, so that:

$$\mathcal{F}\left(H(t)\right) = \mathcal{F}\left(E(t)\right) \bullet \mathcal{F}\left(F(t)\right) \bullet \mathcal{F}\left(J(t)\right) \bullet \mathcal{F}\left(S(-t)\right) \tag{2.23}$$

When written out for each harmonic of the Fourier series, this results in:

$$\begin{aligned} m_{H,h} e^{i\phi_{H,h}} &= m_{E,h} e^{i\phi_{E,h}} m_{F,h} e^{i\phi_{F,h}} m_{J,h} e^{i\phi_{J,h}} m_{S,h} e^{-i\phi_{S,h}} \\ &= m_{E,h} m_{F,h} m_{J,h} m_{S,h} e^{i\left(\phi_{E,h}+\phi_{F,h}+\phi_{J,h}-\phi_{S,h}\right)} \end{aligned} \tag{2.24}$$

We can therefore see that the Fourier series expansion for $H(t)$ is given by:

$$H(t) = 1 + \sum_h 2 m_{F,h} m_{E,h} m_{J,h} m_{S,h} \cos\left[2\pi h f_{cc} t - \left(\phi_{F,h} + \left(\phi_{E,h} - \phi_{S,h}\right)\right)\right] \tag{2.25}$$

The resulting modulation of $H(t)$ for each harmonic h is given by the product of all the component modulations, as:

$$m_{H,h} = m_{F,h} m_{E,h} m_{J,h} m_{S,h} = m_{F,h} m_{IR,h} \tag{2.26}$$

Therefore if we know the modulation of the instrument response, $m_{IR,h} = m_{E,h} m_{J,h} m_{S,h}$, we can extract the modulation of the fluorescence lifetime response, $m_{F,h}$.

The resulting phase of $H(t)$ for each harmonic corresponds to the phase position in the cross-correlation period during which a count synchronous with the excitation clock would be detected in the exact middle of the sampling window, plus the phase offset provided by the fluorescence lifetime response, as follows:

$$\phi_{H,h} = \phi_{F,h} + (\phi_{E,h} - \phi_{S,h}) = \phi_{F,h} + \phi_{IR,h} \tag{2.27}$$

Therefore if we know the relative phase difference between the excitation period and the sampling period, $\phi_{IR,h} = \phi_{E,h} - \phi_{S,h}$, then we can extract the phase offset provided by the fluorescence lifetime response. Both the modulation and the phase of the instrument response can be obtained by measuring a reference sample with a known lifetime value. By measuring $m_{H,h}$ and knowing $m_{F,h}$, the value of $m_{IR,h}$ can be obtained by dividing. Similarly, by measuring $\phi_{H,h}$ and knowing $\phi_{F,h}$, the value of $\phi_{IR,h}$ can be obtained by subtracting. Then in future measurements, these instrument response values can be applied to the measured values to obtain the physical values $m_{F,h}$ and $\phi_{F,h}$ for unknown samples.

Derivations similar to this section have been previously given, such as in [24, 27]. However the digital sampling windows and jitter terms were not included in previous derivations.

2.9 Optimizing Precision

To determine the uncertainty in phasor values, we must find the standard deviation of the measured phase and modulation for each harmonic. We can perform the analysis on the phase histogram $H(p)$, which represents one period of $H(t)$, and where $0 \leq p \leq n_p - 1$. To perform this error analysis, we first plot the cross-correlation phase histogram in polar coordinates for the harmonic of interest. For the first harmonic, this is a plot with $H(p)$ as the radial value, $2\pi p/n_p$ as the phase value, and where $p = n_p$ represents a complete orbit. An example is given in Figure 2.5.

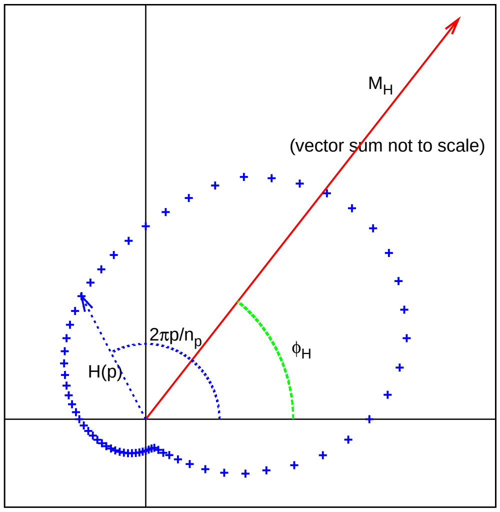

Figure 2.5: The cross-correlation phase histogram bins (crosses) for fluorescein are plotted in polar coordinates, forming $n_p = 64$ vectors. One vector $H(p)$ of the series is identified in the figure. The M_H vector, which represents the unnormalized phase and modulation of the first harmonic, is produced by the vector sum of each vector in the phase histogram series.

In this coordinate system, the Fourier transform for each harmonic can be viewed graphically as the vector sum of the values plotted. $M_h = m_H N$ and ϕ_H are the magnitude and angle of this vector sum. From this graphical representation we can observe the effect of fluctuations in $H(p)$ on the values of m_H and ϕ_H. By the principles of vector addition, ϕ_H will only be affected by fluctuations in $H(p)$ which occur perpendicularly to the vector sum. The variances introduced by each of these components at every value of p can be added linearly. So if we consider the Poissonian error in each bin of $H(p)$ (each bin of this histogram contains independent events), then we obtain the standard deviation in phase as follows:

$$\begin{aligned}
\sigma_{\phi_F,h} &= \frac{1}{m_{H,h}N}\sqrt{\sum_{p=0}^{n_p-1}\left[\sqrt{H(p)}\sin\left(2\pi hp/n_p-\phi_{H,h}\right)\right]^2} \\
&= \frac{1}{m_{H,h}\sqrt{N}}\sqrt{\sum_{p=0}^{n_p-1}\left[\sqrt{1+\sum_{h'=0}^{n_p-1}2m_{H,h'}\cos\left(h'2\pi p/n_p-\phi_{H,h'}\right)}\sin\left(2\pi hp/n_p-\phi_{H,h}\right)\right]^2} \\
&= \frac{\sqrt{1-m_{H,2h}\cos\left(2\phi_{H,h}-\phi_{H,2h}\right)}}{m_{F,h}m_{IR,h}\sqrt{2N}} \qquad (2.28)
\end{aligned}$$

The derivation of the expression for the standard deviation of modulation is similar, except using the fluctuations which are parallel to the vector sum, and taking into account that the modulation is normalized by N, and thus fluctuations will also affect m_H via the contributions of N.

$$\delta m_{H,h} = \delta\frac{M_{H,h}}{N} = \frac{\delta M_{H,h}}{N} - \frac{M_{H,h}\delta N}{N^2} = \frac{1}{N}\sqrt{H(p)}\cos\left(2\pi p/n_p-\phi_{H,h}\right) - \frac{m_{H,h}}{N}\sqrt{H(p)} \qquad (2.29)$$

$$\begin{aligned}
\sigma_{m_F,h} = \frac{\sigma_{m_H,h}}{m_{IR,h}} &= \frac{1}{m_{IR,h}N}\sqrt{\sum_{p=0}^{n_p-1}\left[\sqrt{H(p)}\left(\cos\left(2\pi hp/n_p-\phi_{H,h}\right)-m_{H,h}\right)\right]^2} \\
&= \frac{\sqrt{1-2m_{H,h}^2+m_{H,2h}\cos\left(2\phi_{H,h}-\phi_{H,2h}\right)}}{m_{IR,h}\sqrt{2N}} \qquad (2.30)
\end{aligned}$$

These uncertainty values on phase and modulation can then be propagated through

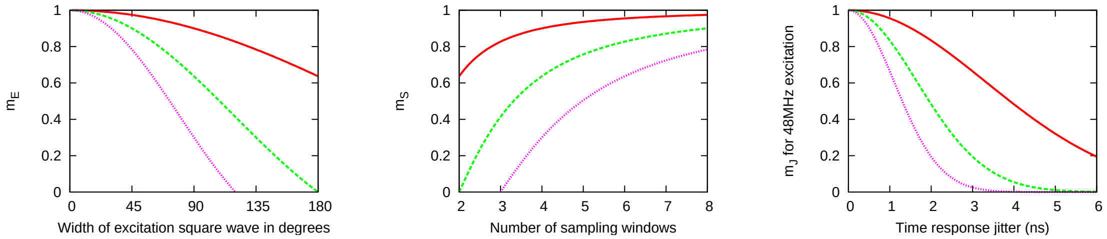

(a) The modulation obtained by a square wave excitation

(b) The modulation obtained by digital sampling windows

(c) Gaussian time-response jitter of a given width

Figure 2.6: Plots showing the contribution to the modulation of the instrument response for the first (solid), second (dashed), and third (dotted) harmonics.

Equations 1.2 and 1.3 to obtain the uncertainties on τ_p and τ_m:

$$\sigma_{\tau_p,h} = \frac{\sigma_{\phi_F,h}}{2\pi h f_{ex} \cos^2\left(\phi_{F,h}\right)} \tag{2.31}$$

$$\sigma_{\tau_m,h} = \frac{\sigma_{m_F,h}}{2\pi h f_{ex} m_{F,h}^2 \sqrt{1 - m_{F,h}^2}} \tag{2.32}$$

From this analysis we can learn several insightful properties about the behavior of the phasor distribution. Firstly, the distribution of both phase and modulation decreases by the square root of the number of counts in the phase histogram acquired at each pixel. Secondly, the distribution of both phase and modulation is inversely proportional to $m_{IR,h}$, the modulation of the instrument response for each harmonic. Since $m_{IR,h}$ ranges from 0 to 1, the value which produces the optimal distribution is when it is equal to 1. From consideration of $m_{IR,h} = m_{E,h} m_{J,h} m_{S,h}$ we can then immediately see that the optimal configuration places each of those component modulation values close to 1. For a square wave excitation of width θ, the modulation values as shown in Figure 2.6a are found by taking the Fourier transform of that square wave, which yields:

$$m_{E,h} = \frac{2}{h\theta} \sin\left(\frac{h\theta}{2}\right) \tag{2.33}$$

Similarly, for the sampling window, as seen in Figure 2.6b, the modulation values are given by:

$$m_{S,h} = \frac{n_w}{h\pi} \sin\left(\frac{h\pi}{n_w}\right) \tag{2.34}$$

For Gaussian system jitter, as seen in Figure 2.6c, the modulation values are given by:

$$m_{J,h} = e^{-2(\pi h \sigma_j f_{ex})^2} \tag{2.35}$$

This analysis allows us to quantitatively evaluate the design parameters required to minimize the distribution of phasors. For lifetime values obtained from the first harmonic, we can see that the modulation, and thus the information content, has reached a plateau with an excitation square wave of 90° or smaller (Figure 2.6a), four or more sampling windows (Figure 2.6b), and system jitter less than 2ns (Figure 2.6c). Improvements beyond this point will make only marginal improvements to the statistical uncertainties of a measurement with the first harmonic.

In our specific system configuration with a 45° square wave excitation, this produces an $m_{ex,1}$ of 0.9745, an $m_{ex,2}$ of 0.9003, and an $m_{ex,3}$ of 0.7842 at the three lowest harmonics. So even though a diode laser driven in this manner has a pulse width as wide as 2.6ns, it will still produce results of equivalent quality to a femtosecond pulsed laser for the first two harmonics.

2.10 Solution Measurements

We evaluated the FLIMBox hardware, phasor analysis, and the above error analysis by performing solution lifetime measurements on a FLIM setup. We prepared fluorescein in a pH 10 solution, which is known to have a lifetime of 4.05ns as determined in cuvette measurements. Then we used this fluorescein solution as our lifetime reference for determining the instrument response, and also as a sample for examining the pixel uncertainty. We then prepared a solution of rhodamine B in water as an additional sample.

Figure 2.4 shows the phasor plots for these two samples. Each image represents a histogram of the phasor values for a 256x256 pixel image excited with a 470nm diode laser at 48MHz on the Olympus FV1000 with FLIMBox setup described above. In both cases, the fluorescein sample was used as the reference. The fluorescein measurement in Figure 2.4a was acquired at 200,000 counts per second, with 40μs per pixel, and pixel phase histograms were accumulated until there were an average of 538 counts in each pixel. Figure 2.4b shows the rhodamine B phasor plot taken on the same instrument, but with 50,000 counts per second and an average of 202 counts per pixel.

2.10.1 Experimental and Theoretical Uncertainty

By using the error Equations 2.28 and 2.30, we calculated the expected uncertainties in both phase and modulation, and we compared these to the experimental standard deviations for the fluorescein and rhodamine B measurements. We found very high correspondence between the theory and experimental results, as shown in Table 2.1. We repeated this comparison with many measurements under various conditions and system configurations, including for data taken with a TCSPC system, and found the equations holding in each case. This confirms that the theoretical uncertainty equations completely account for the precision of the system, and confirms that under real physical conditions, the statistical errors of a lifetime measurement can be correctly evaluated and effectively improved by using the optimized parameters derived from the mathematical model of the DFD method.

We also evaluated the phase and modulation lifetime values and uncertainties of the two measurements. Since the fluorescein measurement is used as a reference it is not meaningful to consider its lifetime value, since these are fixed at 4.05ns by the referencing process. However, we can still consider the uncertainties in these. The

	Fluorescein (pH 10) *(538 counts/pixel)*		Rhodamine B (water) *(202 counts/pixel)*	
	σ_ρ	σ_m	σ_ρ	σ_m
Experimental	3.50°	0.035	3.86°	0.049
Theoretical	3.50°	0.035	3.83°	0.049

Table 2.1: Phase and modulation uncertainty per pixel using the 1^{st} harmonic at 48MHz

fluorescein measurement had a τ_p per pixel of 4.05 ± 0.522ns, and a τ_m per pixel of 4.05 ± 0.379ns. The predicted values for the uncertainties according to Equations 2.31 and 2.32 are 0.505ns and 0.376ns. To avoid skew in the lifetime values, the mean of all lifetime values is not used to determine rhodamine B's mean lifetime. Instead, the lifetime of the center of mass of all the phasors is used, as the phasor addition is linear. For the rhodamine B measurement, the measured τ_p for each pixel was 1.723 ± 0.287ns, and the measured τ_m was 2.001 ± 0.448ns. The predicted uncertainties per pixel are 0.281ns and 0.428ns.

Note that the phasor for rhodamine B (Figure 2.4b) is not exactly on the universal circle, although we expected a single exponential according to our measurement in cuvette. The phasor analysis provides an immediate and intuitive explanation for this result. In this case, the system on which the measurement was taken had background counts of 1500 per second out of a total 50,000 counts per second, which corresponds to a 3% background for the rhodamine B measurement. Since uncorrelated background counts occur with a phasor position at the (0, 0) coordinate, this phasor is linearly combined according to Equations 2.11–2.13 with the phasor for rhodamine B's actual lifetime. This linear combination with the uncorrelated background reduces m and therefore increases τ_m, but not the τ_p value. When the phasor contribution of the uncorrelated background is subtracted from the rhodamine B phasor, the phasor coordinate will move to the universal circle, and τ_m becomes 1.7ns.

If instead of examining the above measurements at each pixel, we use the same data to evaluate the uncertainty of the mean, rather than the uncertainty of each pixel, we find much more statistical precision. The fluorescein measurement then has a phasor point which is determined by 35 million counts, and the rhodamine measurement has a phasor point which is determined by 13 million counts. The uncertainties of the means for the fluorescein lifetimes are then 2.0ps and 1.5ps for τ_p and τ_m. Similarly for rhodamine B the uncertainties of the means are 1.1ps and 1.8ps for τ_p and τ_m. This emphasizes that the precision of lifetime measurement is not constrained by the precision of individual photon arrival times. The precision of the average value is determined by statistics, and therefore is a function of the system parameters and the number of counts. The accuracy of the phasor position determination depends on the stability of the system after it has been referenced with a known lifetime.

To evaluate the long-term stability of our system, we examined the trend of phase and modulation values over the course of hours and days using an excitation modulation of 48MHz. We determined that after an initial 45 minute warm-up period, the phase remained stable within around 0.1°, and the modulation remained stable within less than 0.001 over time periods of hours to days. These correspond to lifetime stability around 10ps for fluorescein, as given by Equations 2.31 and 2.32.

2.10.2 Comparison with TCSPC

For comparison with an existing standard for lifetime measurement hardware, we measured fluorescein with a 443nm diode laser modulated at 48MHz and the FLIM-Box on our FV1000 setup, and with a Becker & Hickl TCSPC card (model 830, Becker & Hickl, Berlin, Germany) connected to a home-built 2-photon system using an 80MHz titanium:sapphire laser. According to our model, when the data are processed in the same way and for the same number of counts, the precision of the determination of the phase and modulation values should only depend significantly on the modulation factors. Since at 80 MHz, the modulation factor for fluorescein is less than at 48 MHz, we anticipated that the precision of the data acquired with

FLIMBox (at 48 MHz) should be better than the precision of data acquired with the B&H card (at 80 MHz). As can be seen in Figure 2.7, the phase uncertainties obtained for the measurement of fluorescein with the FLIMBox is less than that of the TCSPC system under these two sets of conditions. The relevant point here is the demonstration that both data acquisition systems reach the statistical limits in the precision of the measurement of lifetime values, and that the modulation factors and the number of photons fully account for the precision of the measurement.

2.10.3 F Value

Gerritsen et al. [20] define a count-independent metric for the precision of a lifetime measurement as follows:

$$F = \frac{\sigma_\tau}{\tau}\sqrt{N} \qquad (2.36)$$

By inserting Equations 2.31 and 2.32 into Equation 2.36, we are able to obtain the minimum F value (representing the highest sensitivity) for the highest modulation of the instrument response, as shown in Figure 2.8.

2.11 Discussion

We have developed a mathematical framework that provides an understanding of the effect of different parameters in the DFD-FLIM approach. We have shown that the experimental realization

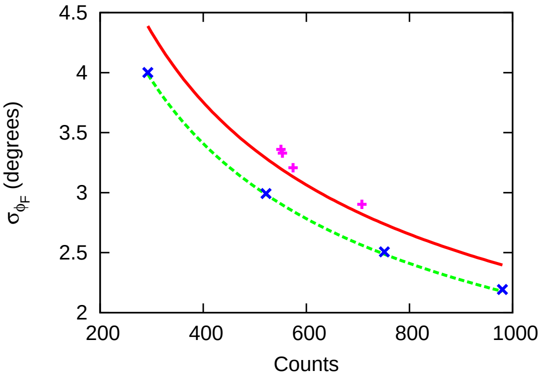

Figure 2.7: A comparison of the phase uncertainty for fluorescein measurements as a function of counts between a Becker & Hickl card Model 830 on an 80MHz 2-photon system (solid line, + symbol) and the FLIMBox on a diode laser system driven at 48MHz (dashed line, × symbol). Per equal counts, the uncertainty for the B&H card is higher than the FILMBox card due to the increased demodulation of the fluorescein signal at 80MHz with respect to 48MHz. However, all the uncertainties are close to the values predicted by the mathematical model when this demodulation is taken into account

of the DFD principle in the FPGA chip gives values in very good accord with the model. This implies that the there are no additional factors (systematic or random) in the hardware implementation which are not accounted for by the mathematical model. As a consequence of the theoretical description, we have determined the system parameters which optimize the precision of phasor distributions and corresponding lifetime values. We have reached these optimal parameters in our implementation of the FLIMBox for a hypothetical system in which the lifetimes values range between 0.1ns and 10ns. We have also shown that using an optical reference for the excitation, the drifts of the physical implementation are very small, giving better than 10ps stability for the measurement of the lifetime of fluorescein at 48MHz.

In this work we provide a statistical framework that correctly predicts the errors in lifetime determination for any given sample and system configuration. Equations 2.28 and 2.30 show that the best precision of the position of the phasor (and of the lifetime value) is achieved when all the modulation factors are close to 1. This corresponds to the well-known principle that given a certain lifetime value, the best precision is obtained when the excitation pulse is narrow and repeats with a period which is much longer than the lifetime, there are a large number of time windows (of the photon delay histogram), and the instrument jitter is small. However, the value of this equation is that it allows us to quantitatively predict how much each of these factors will ultimately affect the precision of the lifetime determination. For example, we can predict that for a lifetime of about 3ns (typical of a GFP), near optimal measurement conditions are obtained at excitation frequencies around 40-50 MHz with pulses of about 1-2ns, using 4 time windows in the DFD implementation and with instrument jitter on the order of 1-2ns. Improving on these conditions will only marginally decrease the error in the lifetime determination.

All factors in Equations 2.33–2.35 have very broad shapes (Figure 2.6) showing that the system performance degrades slowly when we move away from the optimal conditions. Therefore it is possible to design a system which is near optimal over a relatively broad range of lifetime values. This evaluation resulted in the design of the very simple and cheap system of data acquisition for FLIM presented in this chapter.

2.11.1 Jitter

A striking difference between the DFD and TCSPC approaches is the small number of time windows used in DFD (four windows) with respect to the relatively large number of time bins used in TCSPC when applied to FLIM (64 bins or more). At first sight it would appear that the small number of windows in the DFD approach will limit the capability of measuring very short lifetimes since each window is several nanoseconds wide. However, the presence of jitter and the sliding window principle makes the measurement of very short lifetime possible and the errors are comparable to the state-of-the-art TCSPC systems.

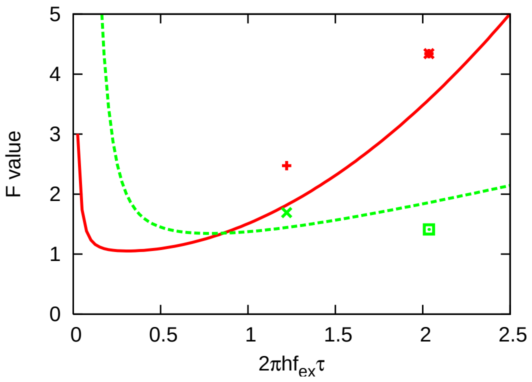

Figure 2.8: The theoretical minimum F values for τ_p (solid line) and τ_m (dashed line) are shown as a function of $2hf_{ex}\tau$ for instrument response modulation values of 0.99. The $+$ and $\times$ symbols show the F values for the τ_p and τ_m of fluorescein in pH 10 solution taken with the FLIMBox at 48MHz, while the $*$ and $\square$ symbols show the F values for the same sample measured with the TCSPC system at 80MHz. The F value for τ_m of the TCSPC measurement is anomalously low due to a clustering of the modulation values resulting from the dead zones at the edges of the card's phase histogram.

In our mathematical model of DFD, jitter was presented as a phenomenon which reduces modulation, and therefore reduces statistical accuracy. While this is true, there is also a substantial benefit of having a small amount of jitter in a system. To maintain the ability to measure very short lifetimes, it is necessary for a short lifetime response to be oversampled, so that even very small lifetime changes show up as a response in several bins of the phase histogram as shown schematically in Figure 2.9. This oversampling can be provided by the shape of the excitation pulse and/or by the jitter of the detection electronics. Depending on settings (laser, PMTs etc), we measured the jitter on the FV1000 system with the FLIMBox to range from 0.82ns to 2ns.

This jitter, according to Equations 2.33–2.35, results in modulation values ranging from 0.95 to 0.84 for the first three harmonics. The FLIMBox produces 256 bins in the phase histogram, but for memory conservation this is usually binned down to 64. This amount of jitter corresponds to an oversampling by around 3-6 bins, providing increased sensitivity to small lifetime values, with minimal expense in uncertainty. If the jitter is too large, resulting in oversampling by a large number of bins, then the precision of the measurement will reduce according to the modulation value (Equation 2.35) for that jitter.

The effect of jitter on the determination of very short lifetime values is more complex than appears solely from Equation 2.35, due to the effect of limited count statistics in any real measurements. According to Figure 2.9, in the absence of jitter, there is always a probability that some counts will appear in bin 2, although the majority of the counts will be in bin 1. The amount of counts in bin 2 will also depend on the precise position of the time of photon arrival inside bin 1. Therefore, if we have only a limited amount of counts, statistically we could have either no count in bin 2 or just a few counts. These discrete statistics produce a “pixelation” (in the phasor plot) of phasors corresponding to very short lifetime values. The presence of jitter reduces this “pixelation”, providing a continuum of phasors centered at the correct phasor position (an equivalent effect is also present in the TCSPC approach). The important point here is that the resolution of very short lifetimes is improved and the error is reduced by the presence of a small amount of jitter, and that the ultimate lifetime resolution of the DFD system is only a matter of count statistics. The effect of the count statistics on the resolution of lifetimes can be precisely determined using the mathematical model and therefore a direct quantitative comparison between the DFD and TCSPC method could be done for any given implementation of the two methods.

2.11.2 APDs

This insight about jitter reveals new possibilities for lifetime measurement. PMT-based systems usually have a quantum efficiency of around 25% (up to 40% for the GaAs modules), while avalanche photodiode (APD) based systems can have quantum efficiencies of over 60%. These APDs are usually avoided for lifetime measurements because they have a time response jitter on the order of a nanosecond. According to our model, the additional jitter of the APDs will have very little influence on the precision of lifetime measurements. This reveals that DFD-FLIM using APDs can actually yield an overall improvement in lifetime resolution due to the larger number of photons detected.

This also means that the higher quantum efficiency of APDs can be used under extreme low-count conditions, such as in a single molecule experiment. This analysis shows that, since the uncertainty contributed by an APD's jitter is negligible, sufficient photons for a phasor analysis can be obtained in less than half the time when using APD detection, which would enable the observation of more rapid processes. The implications of this will be discussed in more detail in Chapter 3.

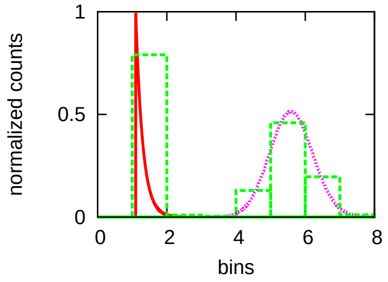

Figure 2.9: With pulsed excitation, in the absence of jitter, a lifetime value much shorter than the bin size gives "delays" all in the same bin so that small changes in lifetime result in identical histograms. The solid curve at bin 1 represents this case in which the center of mass of the distribution cannot be determined with a precision better than the bin size. In the presence of jitter, the broadening of the distribution of delays gives different bin contents even if the changes in lifetime are very small. The dotted curve, which is the convolution of the solid curve with a Gaussian jitter, shows that bin 4 contains less counts than bin 6 so that the center of mass of the distribution can be determined with precision better than the bin size.

2.11.3 Excitation

Our mathematical model shows that an excitation source with a pulse narrower than 90° of the repetition period is near optimal. Further reduction of the excitation pulse width only results in marginal improvement of the precision of the measurement. The DFD method, by virtue of being a frequency domain method, only works with periodic excitation. This is usually the case using pulsed lasers, however the model shows that the narrow pulses from picosecond or femtosecond lasers are not a requirement for FLIM and do not provide substantial benefit over properly modulated diode lasers in the sub-nanosecond regime.

2.11.4 Sampling

The DFD approach increases the duty cycle of the detection to 100% as compared to the 50% duty cycle of the analog FD method. Furthermore, the 4-window design reaches the plateau in terms of measurement precision for the first harmonic, and provides a modulation of 64% for the second harmonic.

There is a practical reason why we cannot increase the number of time windows to a much larger number. This is due to the maximal internal frequency of operation of the FPGA chip. For example, to achieve 4-window operation at about 50 MHZ, we need to generate a frequency in the chip which is factor of four larger, i.e., 200MHz. To increase the number of windows by another factor of 2 we would need to generate a frequency of 400MHz, which is above the maximum limit of the specific FPGA we have used.

Other faster chips are commercially available and eventually the precision of the DFD method could be improved. However, according to Figure 2.6b, the improvement obtained by the 8-window design with respect to a 4-window design is marginal. Of course, if the laser repetition frequency is much lower than 50 MHz (for example 20 MHz), we could increase the number of sampling windows in the FPGA chip accordingly.

2.11.5 Correlation

Measurements were also taken which confirm the ability of the FLIMBox to take Fluorescence Correlation Spectroscopy (FCS) measurements at rates up to the sampling rate, however these will be omitted for brevity. These measurements help confirm the correct functioning of the FLIMBox hardware for the observation of dynamic behavior.

2.11.6 Saturation and Dead-time

The TAC-based system we used (B&H model 830) has a 125ns dead time. The dead time limitation becomes particularly relevant in FLIM when the laser samples a very bright pixel, or in a point lifetime measurement during a very bright burst. Saturation not only results in lost counts, but can induce significant skew on the lifetime values. Using several TAC-based cards in parallel removes this limitation but at a very high cost.

The FLIMBox hardware collects data at a maximum speed of one count per sampling period, which for the above system corresponds to one photon every 20.75ns. There is also a fundamental limit in count rate due to the dead time of the discriminator, which is around 10ns. One bottleneck of the particular FPGA we used is the size of the FIFO buffer connected to the USB interface, which limits the average (not the burst) count rate to about 2 million cps.

2.11.7 Conclusion

In conclusion, DFD-FLIM provides a powerful new technique for obtaining lifetime images with a signal-to-noise and lifetime measurement ability comparable to the leading techniques in the field, yet with significantly reduced hardware expense. The reduced component expense of DFD-FLIM means the technique easily scales to multiple lifetime channels. In addition, the theoretical model we developed reveals the system parameter values which must be chosen to optimize the efficiencies of photons for phasor analysis. When DFD-FLIM is combined with the phasor analysis methods, the resulting pair can make lifetime techniques accessible and practical for a wide variety of researchers and applications.

Chapter 3

Phasor Trajectory Analysis

3.1 Overview

This chapter presents a new extension of phasor analysis to the construction of time trajectories representing fast lifetime dynamics. Specific attention is given to the analysis of FRET efficiency changes by merging lifetime information from both donor and acceptor channels into a single FRET trajectory. Also, the uncertainty analysis from Chapter 2 is extended here to the analysis of phasor trajectories, and the implications of this for single molecule experiments are examined with both analytical consideration and simulation.

3.2 Calculating a Phasor Trajectory

If we consider the phasor values obtained during bursts from single molecules, then we can observe FRET dynamics within these bursts without resorting to any fitting process. To do this we need a mathematical framework for calculating phasor trajectories, and we need a mathematical framework for extracting FRET efficiencies from these phasor trajectories.

In the case of freely diffusing fluorophores or FRET constructs in low concentration, we are interested in the rare high intensity bursts of counts which correspond to the times when a fluorophore has entered the focal volume. Therefore the analysis only needs to consider time periods with counts exceeding a threshold, and for which the burst duration is significantly greater than the timescale of transitions. We are then interested in determining the phasor positions within and during these time periods.

Since we want to observe FRET dynamics on a millisecond timescale, we do not want to simply bin the photons and perform an ordinary phasor calculation on a sequence of bins treated as pixels, since this would unnecessarily reduce our temporal resolution. Instead, we can take advantage of the linear addition of phasors by considering each photon as a separate phasor, combining this information using the vector properties of phasors, and extracting the FRET information present in the lifetime information of both acquisition channels.

The phasor coordinates, g and s, are the intensity-normalized cosine and sine terms of the first harmonic of the Fourier transform of the data, related to the modulation and phase values, m and ϕ, by the trigonometric relations (See for example: [24]):

$$g = m\cos(\phi) \tag{3.1}$$

$$s = m\sin(\phi) \tag{3.2}$$

Using this representation for lifetime information yields two important properties. First, due to the linear properties of a Fourier series, phasor coordinates add linearly as vectors when multiple components are contributing to a single emission. And second, due to the convolution theorem, convolution and deconvolution become a simple rotation and scaling in the phasor space. Using these two properties, we are able to combine the lifetime information from both donor and acceptor channels, and we are able to extract a time series of FRET efficiency values.

To extend phasor analysis to a time sequence analysis suitable for low count conditions, we can begin by defining the fundamental phasor components corresponding to each single photon count. Each photon count detected by a lifetime acquisition system occurs as part of a periodic function with n_p bins, which we will index with the bin number p. If a Fourier transform is taken of a single count, it yields a g and

s coordinate corresponding to the cosine and sine values of the phase value corresponding to p. To deconvolve the instrument response, we must perform a scaling and rotation by dividing by the modulation of the instrument response, m_{IR}, and rotating clockwise by the phase of the instrument response, ϕ_{IR}. as described in Equations 2.26 and 2.27. This yields a set of n_p fundamental phasors as shown in Figure 3.1 and given by:

$$g_F = \frac{1}{m_{IR}} \cos\left(2\pi p/n_p - \phi_{IR}\right) \tag{3.3}$$

$$s_F = \frac{1}{m_{IR}} \sin\left(2\pi p/n_p - \phi_{IR}\right) \tag{3.4}$$

Since each count obtained is mapped to one of these fundamental phasor locations, this means that every phasor position which can be measured is a linear combination of these fundamental phasors, weighted according to the number of photons received in each bin. Since the coordinates for the phasors add linearly, obtaining a time sequence of phasor values is a simple matter of performing a normalized moving average over the time sequence of fundamental phasors. We obtain the phasor trajectory by performing a Gaussian-weighted moving average on the time sequence of g_F values, and on the time sequence of s_F values, yielding a phasor tra-

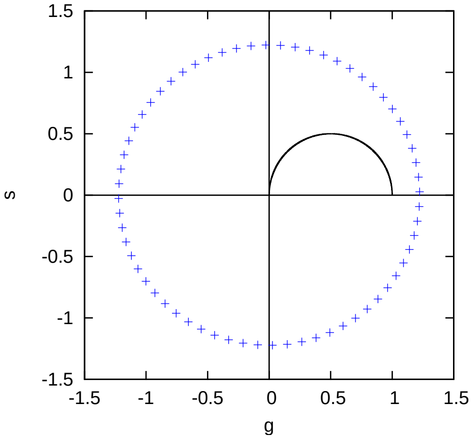

Figure 3.1: Each bin in the phase histogram is mapped to a single fundamental phasor position (crosses) determined by the instrument response, so that as single photon counts arrive, they can each be assigned to a phasor position. The universal circle representing single-exponential lifetimes is shown as a curved solid line.

jectory of $(g(t), s(t))$ coordinates as follows:

$$g(t) = \frac{\sum_{t'} g_F(t') e^{-\pi(t'-t)^2/r_s^2}}{\sum_{t'} e^{-\pi(t'-t)^2/r_s^2}} \tag{3.5}$$

$$s(t) = \frac{\sum_{t'} s_F(t') e^{-\pi(t'-t)^2/r_s^2}}{\sum_{t'} e^{-\pi(t'-t)^2/r_s^2}} \tag{3.6}$$

where r_s is the resampling time scale, and t' is summed over each photon count in the time sequence. The resampling timescale is defined such that count rate c yields an average of N photons for each point along the time sequence, as given by:

$$N = r_s c \tag{3.7}$$

This value of N corresponds to the average value of the denominator in Equations 3.5 and 3.6, and also corresponds to the number of photons used for the uncertainty analysis in Section 3.5.

3.3 Obtaining a FRET Trajectory

To study the dynamics of a FRET construct with a phasor trajectory, we must be able to map each phasor value to a corresponding FRET efficiency value. This is done by projecting the phasor trajectory onto the ideal FRET curve, which is defined as the sequence of phasor positions for the donor over the entire range of possible FRET efficiency values, and in the absence of background. For single-exponential fluorophores this is particularly easy, since the donor's lifetime remains a single-exponential lifetime even in the presence of FRET. Therefore, the ideal FRET curve for a single-exponential donor falls on the universal circle given by Equation 2.14. In this case, the values can be projected as shown in Figure 3.2. This is mathematically equivalent to using the standard τ_p value given by:

$$\tau_{DA}(t) = \tau_p(t) = \frac{s(t)}{2\pi f_{ex} g(t)} \tag{3.8}$$

where f_{ex} is the excitation frequency. This is then plugged into the FRET efficiency formula:

$$E(t) = 1 - \frac{\tau_{DA}(t)}{\tau_D} \tag{3.9}$$

where τ_D is the lifetime of the donor without the acceptor. This provides us with a FRET trajectory which utilizes the lifetime information from the donor channel, but to maintain precision across the entire range of FRET values, we must also include the lifetime information from the acceptor channel.

3.4 Combining the Donor and the Acceptor

There are many FRET constructs that have a high FRET efficiency in one or more states, meaning that a large portion of the photons emitted by those constructs are emitted by the acceptor. Under low count conditions, it becomes critical to use these acceptor counts when a significant portion of the the total photons are in the acceptor channel. The ability to examine FRET constructs with a phasor trajectory analysis can therefore be greatly improved by including the photons from the acceptor's emission in the analysis.

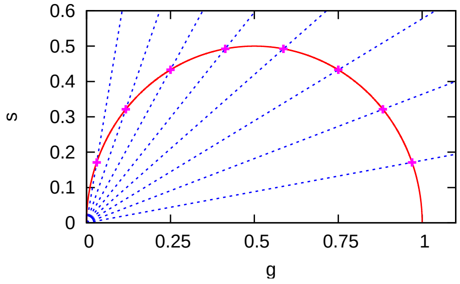

Figure 3.2: For single exponential lifetimes with small background contributions, phasor values can be projected along the dotted lines to the universal circle to determine a single FRET efficiency value for each phasor value.

The differential equation describing the population of the donor's excited state can be written as:

$$\frac{dD(t)}{dt} = k_E E(t) - (k_{FD} + k_T)\, D(t) \tag{3.10}$$

where k_E, k_{FD}, and k_T are the rate constants for excitation, fluorescence emission, and resonance energy transfer. Similarly, the differential equation describing the population of the acceptor's excited state in the presence of FRET and with no direct excitation can be written as [6, 5, 27]:

$$\frac{dA(t)}{dt} = k_T D(t) - k_{FA} A(t) \tag{3.11}$$

We know from the frequency domain analysis as described in Chapter 2, that the fluorescence response of the donor fluorophore is provided by the convolution of the excitation term (from the positive component in the donor equation) and the decay term (from the two negative components). By analogy we then immediately know that the functional form of the acceptor's emission is given by the convolution of the excitation term which comes from $k_T D(t)$, and its decay term ($k_{FA}A(t)$) which corresponds to the normal fluorescence lifetime of the acceptor if excited directly.

The value we are trying to obtain is the FRET efficiency, and this value is present in the lifetime of the donor as shown by Equation 1.1. The emission of the donor is proportional to $D(t)$, and therefore the emission of the donor is proportional to the rate of acceptor excitation by energy transfer. Therefore, to extract the FRET efficiency from the emission of the acceptor, we must deconvolve the emission of the acceptor using the acceptor's normal lifetime given by $\tau_A = 1/k_{FA}$, so that only the donor's lifetime remains. (A more general analysis including other energy pathways does not change this result.)

Expressed in the phasor space, this process is made very easy by the convolution theorem, and is nearly identical to the process of accounting for the instrument response. The phasor position of the acceptor emission(H subscripts) is given by the convolution of the donor's decay curve (D subscripts) with the acceptor's response if it were excited directly (A' subscripts), as shown by:

$$m_H(t) = m_D(t) m_{IR} m_{A'} \tag{3.12}$$

$$\phi_H(t) = \phi_D(t) + \phi_{IR} + \phi_{A'} \tag{3.13}$$

Since the phasor representation of this convolution is given by these simple algebraic relations, we can extract the desired information by operating on these vectors. By dividing out the instrument response and acceptor lifetime modulation values, and by subtracting out their corresponding phase values, we translate every count in the acceptor channel into a corresponding donor phasor.

While probes and filters are usually chosen such that donor bleedthrough into the acceptor channel is small (usually less than 15%), a correction process can be performed to achieve the physically correct donor phasor from the acceptor channel in the presence of bleedthrough. If the bleedthrough counts in the acceptor channel are a fraction b of the counts in the donor channel, an unnormalized acceptor-only phasor is first generated by subtracting the bleedthrough portion off as follows:

$$N_{A,only} g_{A,only}(t) = N_A g_A(t) - b N_D g_D(t) \tag{3.14}$$

$$N_{A,only} s_{A,only}(t) = N_A s_A(t) - b N_D s_D(t) \tag{3.15}$$

After this, the deconvolution for the acceptor's lifetime is performed, and the subtracted bleedthrough counts are added back on, and the phasor is normalized, yielding all the donor phasor information present in the acceptor channel.

After completing this vector-based deconvolution, we use the linear properties of phasors to add the donor phasors from the donor channel with the donor phasors from the acceptor channel, and obtain a single FRET efficiency trajectory which combines the lifetime information from both donor and acceptor channels. This combined FRET trajectory is dominated by donor channel counts when the FRET efficiency is low, and dominated by acceptor channel counts when the FRET efficiency is high, allowing it to trace out the full range of FRET efficiencies.

3.5 Uncertainty Analysis

The full analytical uncertainty equations for a phasor analysis are given in Section 2.9. To extend these to PTA, we must consider the impact of the Gaussian-weighted moving average from Equations 3.5 and 3.6. This can be analyzed in full by considering a generalized uncertainty value, σ, and propagating it through a Gaussian-weighted moving average. This results in:

$$\sigma_{PTA} = \sqrt{\frac{\sum_{t'} \left(\sigma c e^{-\pi(t')^2/r_s^2}\right)^2}{\sum_{t'} c e^{-\pi(t')^2/r_s^2}}} \tag{3.16}$$

$$= \sigma \sqrt{\frac{1}{N} \sum_{t'} c e^{-2\pi(t')^2/r_s^2}} = \sigma \sqrt{\frac{1}{N} \frac{N}{\sqrt{2}}} \tag{3.17}$$

$$= \frac{\sigma}{2^{1/4}} \tag{3.18}$$

Therefore, each phasor uncertainty equations from Section 2.9 must simply be divided by $2^{1/4} \approx 1.19$ to determine the corresponding uncertainty equations after the moving average operation. For example, the expression for the phase uncertainty can be obtained from Equation 2.28 as follows:

$$\sigma_{\phi,PTA} = \frac{\sqrt{1 - m_{H,2h} \cos\left(2\phi_{H,h} - \phi_{H,2h}\right)}}{m_{F,h} m_{IR,h} 8^{1/4} \sqrt{N}} \tag{3.19}$$

This then results in an uncertainty for τ_{DA} analogous to Equation 2.31:

$$\sigma_{\tau_{DA},h} = \frac{\sigma_{\phi,PTA}}{2\pi h f_{ex} \cos^2\left(\phi_{F,h}\right)} \tag{3.20}$$

To find the uncertainty for the determination of FRET efficiency, we must propagate the uncertainty of τ_{DA} through Equation 3.9, which yields the following:

$$\sigma_E = \frac{\sigma_{\tau_{DA}}}{\tau_D} \tag{3.21}$$

The expression for uncertainty in the acceptor channel is identical, except that the modulation and phase values for the acceptor's lifetime are included with the instrument response values, yielding:

$$\sigma_{m_F,A,h} = \frac{\sqrt{1 - 2m_{H,h}^2 + m_{H,2h}\cos\left(2\phi_{H,h} - \phi_{H,2h}\right)}}{m_A m_{IR,h} 8^{1/4}\sqrt{N}} \tag{3.22}$$

$$\sigma_{\phi_F,A,h} = \frac{\sqrt{1 - m_{H,2h}\cos\left(2\phi_{H,h} - \phi_{H,2h}\right)}}{m_A m_{F,h} m_{IR,h} 8^{1/4}\sqrt{N}} \tag{3.23}$$

By inserting representative values, we can evaluate the level of counts required for PTA. For example, if considering a donor with a lifetime of 4.2ns, which in the presence of FRET has its lifetime reduced to 1ns, and we desire an uncertainty in FRET efficiency of 0.12, then inserting the values for the FLIMBox system which will be utilized in Chapter 4 yields a requirement of only 18 donor counts. Therefore we can reasonably choose a threshold as low as 20 counts per measurement time period. If we insert $N = 20$ into Equation 3.7 with a desired r_s timescale of 1ms, then we can determine that we require single molecule burst count rates exceeding 20,000 cps during the time of observation.

In Section 2.11 it was noted that the typical 1ns jitter of APDs has a negligible contribution to the precision of a lifetime determination with a phasor analysis, and this conclusion applies equally to PTA. However, the increased photon counts (N) due to the higher quantum efficiency of the APD will result in a significant improvement in overall precision. This becomes particularly important since the goal is to use PTA for single molecule analysis, where there are very few photons emitted. While using an APD-based system for the labeled calmodulin sample described in Chapter 4, we were able to obtain burst count rates on the order of 40,000 cps. This count rate is twice the threshold derived above for observing millisecond dynamics, and thus shows from analytical consideration that the approach yields adequate precision for the experimental conditions.

This also shows that this analysis could not be performed using a detector with significantly lower quantum efficiency without a corresponding increase in fluorophore emission. Therefore, the system parameter insights obtained from the analysis of Section 2.9 were critical to the design of an experimental setup which achieves a sufficient number of counts to observe millisecond timescale dynamics under single molecule conditions.

3.6 Simulation

To verify the PTA approach we developed a simple model simulation which generated lifetime data and analyzed it using PTA. We simulated a single-exponential donor with a lifetime of 4.2ns attached to a FRET construct with an R_0 of 6.5nm. A perturbed damped harmonic oscillator was used to emulate the distance fluctuations of a FRET construct. For the simulation, instrument response modulation values of 1 were used, since this provides the most general information. Equations 2.28 and 2.30 show exactly how the precision is reduced for other modulation values.

The simulations showed that in the most ideal case, a minimum threshold for obtaining useable information occurs around $N = 5$, as with the example in Figure 3.3a. For N values less than this, the fluctuations due to noise were too large to discern the dynamics of the simulated FRET construct. As N reaches 20, the uncertainty in the ideal case becomes quite small as shown in Figure 3.3b.

Note that in Figure 3.3a, there are brief moments with non-physical distance values. These correspond to non-physical negative FRET efficiency values which occur when, due to statistical fluctuation, the measured donor lifetime is greater than the unquenched donor lifetime. These short non-physical states are also present in

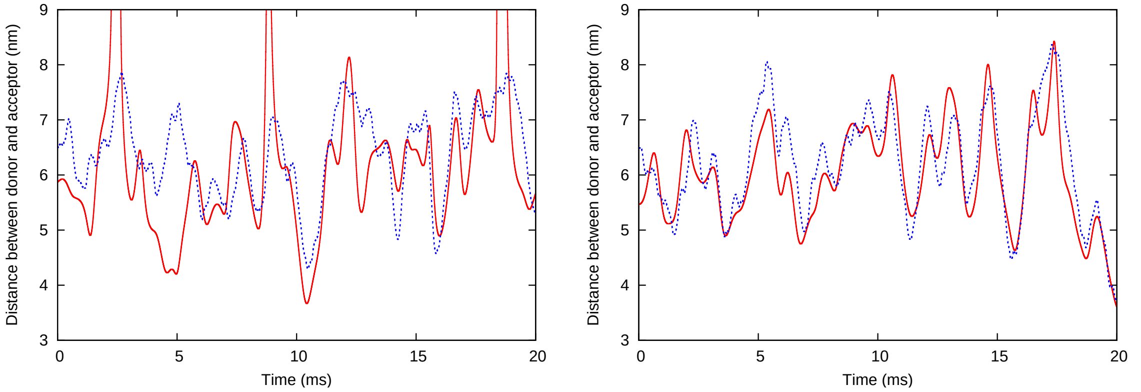

(a) 10,000 counts per second, $r_s = 500\mu s$ (b) 40,000 counts per second, $r_s = 500\mu s$

Figure 3.3: The dotted line shows the distance between the FRET constructs as simulated with a damped harmonic oscillator, while the solid line shows the FRET distance obtained from the phasor trajectory.

experimental PTA trajectories due to statistical fluctuation, and show up as negative FRET efficiency values.

We also ran simulations which generated counts in an acceptor channel to confirm the validity of the acceptor analysis method, and found identical correspondence to that from the donor channel, but with reduced precision as predicted.

To interpret this data, we must consider both the measurement precision as determined by the modulation of the instrument response, and the reduction in precision obtained for the portion of counts obtained from the acceptor channel, as discussed above. Together, these will reduce the precision by approximately 30% for a system with total m_{IR} of around 0.85, and an acceptor lifetime around 4ns. Looking back to Equations 2.30 and 2.28, we can recall that precision scales with the $\sqrt{N}$. Using this information we can see that the 5 count simulation (Figure 3.3a) under the ideal conditions corresponds to around a 10 count threshold under experimental conditions, and the 20 count simulation (Figure 3.3b) corresponds to around a 40 count threshold. Therefore the simulation plots show the range of correspondence to actual values which can be expected from a PTA analysis under experimental conditions with those count levels.

These simulation results correspond to the analytical derivation of expected uncertainty, and show that the PTA algorithm yields FRET trajectories which correctly track the FRET efficiency values corresponding to the physical system.

3.7 Discussion

Since a burst count rate of 40,000 cps is a reasonable number that we have observed on our system with APDs, we can now deduce from both analytical considerations and simulation that FRET dynamics on the scale of 500μs and longer should be observable with a phasor trajectory analysis at that count rate.

From the analytical uncertainty equations, we also conclude that improvements beyond this are constrained primarily by the number of counts. Since, as shown in Section 2.9, the system parameters used here are at the optimal precision level, the remaining parameter which can be improved is the count rate from the sample. Equation 3.7 shows that for a desired precision, the timescale which can be analyzed with PTA is inversely proportional to the number of counts. This means that improvements which increase the excitation laser intensity, detection efficiency, or quantum yield of the fluorophore would yield a corresponding improvement in the timescale observable.

A fundamental physical limit of this is given by the saturation of the fluorophore. If we assume a typical 4ns fluorophore excited with an excitation pulse sufficiently narrow to avoid non-linearities in the lifetime response due to saturation, then a maximum reasonable rate with a 100% detection efficiency is around 50 million counts per second. This exceptionally ideal case yields 1250 times more counts than our current system, which would correspond to analysis of dynamics on a timescale of 400ns. Therefore, while difficult to implement, it is theoretically conceivable that PTA could be extended in the future to observe dynamics as short as sub-microsecond.

Chapter 4

Conformational Dynamics of Calmodulin

4.1 Overview

In this chapter, the developments of Chapters 2 and 3 are applied to a single molecule study of the conformational dynamics of calmodulin in various environments and in the presence of binding partners. The two-channel lifetime acquisition hardware from Chapter 2 is used with APD detectors, and the single molecule bursts from the resulting data are analyzed using the phasor trajectory analysis from Chapter 3. Several new analysis techniques are presented which use the FRET trajectories to extract useful information, such as a rise-fall histogram analysis which extracts the timescales of dynamic behavior, and a moment analysis which uses the analytical uncertainty equations from Chapter 3 to examine the fluctuations due to physical changes in conformation.

The results obtained from these techniques are used to construct a detailed model of calmodulin's conformational dynamics and its interactions with binding partners. The results are also used to help answer open questions about the mutual interactions between these conformational dynamics and the binding processes which occur during calcium signaling.

4.2 Introduction

Calmodulin (CaM) is a protein found in all eukaryotic life which binds to calcium and facilitates the role of calcium as a biological signaling molecule [8]. While CaM has been studied extensively, there are a number of open questions regarding the conformational basis behind CaM's calcium signaling behavior and the mechanisms of exchange between competing binding targets.

It has been observed that the number of calcium ions which are bound to CaM, and the domain to which they are bound, significantly influences competitive binding [40]. Using two-photon fluorescence correlation spectroscopy (FCS), Kim et al. showed that increased calcium availability in a cellular environment increases the portion of CaM which is bound to Ca^{2+}/calmodulin dependent protein kinase II (CaMKII), a major CaM binding target [26]. Sanabria et al. also used Raster Image Correlation Spectroscopy (RICS) in cells to show that a significant majority of CaM is already bound to a binding target, yet upon changing the calcium concentration, the amount which is bound to CaMKII in the cytoplasm changes significantly [38]. Combined, these studies show that CaM experiences calcium-dependent competitive binding between its binding targets, while at the same time there are very low levels of free CaM in the cellular environment. A significant remaining question is then, how does a change in calcium result in CaM switching between competing targets, when there are very low levels of free CaM which can engage in binding?

One possibility is that CaM rapidly switches between different protein partners when the external calcium concentration is changed. However, this explanation is further complicated by the observation that CaM experiences trapping while bound to CaMKII by a multi-step process where CaM first experiences a conformational change due to calcium binding, then after binding with CaM, CaMKII experiences a sequence of conformational changes which increase its affinity for CaM [45]. This also leaves the question: How do the dynamic conformational changes of CaM affect the binding and unbinding of CaM with its targets, and how do the targets in turn affect the response of CaM to calcium concentration changes?

These outstanding questions relating the conformational dynamics of CaM with its binding processes highlight the value of a methodology which permits the direct observation and analysis of the fast conformational dynamics of CaM. It has been shown that sensors based on Förster Resonance Energy Transfer (FRET) can distinguish the major conformations of CaM, and that they can be used to detect the difference between the calcium-bound and calcium-free forms of CaM [41]. In this chapter, we use a single molecule approach to study the changes in FRET which occur upon different arrangements of bound calcium and in different environments.

NMR experiments have been used to study the calcium binding kinetics of CaM [3, 43], but as they were ensemble measurements they were unable to observe the full dynamic nature of the process. Single-molecule intensity-FRET experiments have rigorously characterized the shifts in the distribution of conformations as a function of environmental conditions, but have not shown the state transitions which correspond to these distributions [41]. A recent interesting approach with a microfluidic mixer has observed two timescales of calcium binding, but this method was only able to observe the changes of the average population in one direction as the calcium concentration was changed [35]. Therefore, for a more complete understanding we desire a single molecule approach which enables the direct observation of the full time sequences of CaM's conformational transitions.

Lifetime-based measurements of FRET offer a number of advantages over intensity-based approaches for single-molecule experiments, similar to the advantages which are commonly noted for images. At a basic level, a lifetime approach makes new probe choices possible, since donor-only measurements can be conducted with non-fluorescent acceptors. But there are also several critical experimental advantages which make the approach more resilient to systematic errors.

A lifetime measurement of FRET is more resistant to irregularities in the intensity profile, which can be especially important for the case of freely diffusing particles. If the detection point-spread functions (PSFs) for the donor and acceptor have offsets in their overlap due to detector alignment or chromatic aberration, then the diffusion of the particle through different regions of the PSF will manifest as a dynamic fluctuation in the FRET value for intensity-ratio measurements. For a lifetime measurement, this will manifest only very weakly as a change in the bleedthrough contribution of the acceptor channel.

Also, lifetime based methods are much more resilient to background contributions. While background counts contribute in the same direction as FRET for intensity measurements, for the phasor analysis presented in this work, background and cell autofluorescence typically have a low modulation value, which makes their contribution perpendicular to the direction of the FRET trajectory in the phasor plot. This facilitates a wider range of experimental conditions under which a single-molecule FRET measurement could be considered. Specifically, this opens the possibility for this technique to be used for single molecule measurements within a cellular environment, which could provide a unique characterization of the interactions of CaM under physiological conditions.

In solution, with an absence of protein partners to which CaM can bind, we show below that CaM displays a dynamic behavior with rapid transitions between FRET states which correspond to different arrangements of bound calcium. In the presence of other proteins to which CaM can bind, we expected that these conformational fluctuations would be inhibited or at least strongly modified. Following this reasoning, we also present results which show that in the presence of a CaMKII-derived peptide which emulates CaMKII's binding behavior, CaM's conformational fluctuations are significantly altered showing the suppression of one domain's motion. Therefore this technique allows the direct observation of changes to the conformational dynamics of CaM which result from interactions with binding partners, which includes both calcium ions and binding targets such as protein kinases.

To accomplish this goal of understanding the binding processes which contribute to the signaling behavior of CaM, we require a method which allows direct observation of the dynamic behavior of the protein under single-molecule conditions. We utilize a new fluorescence lifetime analysis approach called a Phasor Trajectory Analysis

(PTA), as presented in Chapter 3, which permits the observation of FRET changes under single-molecule conditions and on a millisecond timescale. In addition, we show that the temporal information obtained by this approach allows the determination of a conformational and molecular basis for the dynamic behavior of CaM.

4.3 Calmodulin Sample

A sample of CaM labeled with a FRET pair was provided by E. Shane Price and Carey Johnson in the manner described in [1]. This sample was labeled on residues 34 and 110, with Alexa 488 ($\tau = 4.2$ns) as a donor, and Texas Red ($\tau = 4.7$ns) as an acceptor, yielding a Förster radius (R_0) of 4.5nm. This FRET construct allows the conformational changes of calmodulin to be observed on the nanometer scale.

4.4 Experimental Setup

We acquired the data using the two APDs on a Zeiss Confocor 3 (Jena, Germany), a 470nm diode laser from ISS (Champaign, IL) modulated at 48MHz with a pulse width of 60°, and using the DFD lifetime hardware described in Chapter 2. For donor emission we used a 505-540nm filter, and for acceptor emission we used a 615-680nm filter.

The choice of using APDs was critical to the success of the experiment, given the low number of emitted photons which were available. This was shown to be the ideal choice by the theoretical considerations found in the uncertainty analysis of Section 3.5. Also, the usage of the FLIMBox detection electronics was essential to the success of the experiment because this provided the availability of two fully parallel lifetime channels with optimal efficiency. Only with two lifetime channels could we make full use of the available lifetime information over the full range of FRET efficiencies by using the method described in Section 3.4.

4.5 Preliminary Data in Sucrose

With a preliminary diffusion measurement, we determined that free CaM diffuses through the focal volume on a millisecond timescale. Therefore, to observe an extended time sequence of millisecond timescale dynamics, we must either attach CaM to a surface, or slow the diffusion. Slowing the diffusion is a much more convenient choice, because this allows the observation of thousands of CaM molecules in a relatively short time period.

For a preliminary approach to slowing the diffusion of CaM through the PSF, we prepared a buffer with 40% sucrose to increase the viscosity and slow the diffusion of calmodulin. This slowed the diffusion sufficiently that the calmodulin stayed in the focal volume for around 30ms at a time. We then prepared a 1nM concentration sample of calmodulin in this 40% sucrose buffer, so that only rarely would a calmodulin molecule enter the focal volume, allowing each molecule to be observed independently as a single-molecule event.

The results can be seen in Figure 4.1. Since these are experimental measurements we do not have the luxury of comparing the results with the known distance as with the simulation. Instead we can examine the correspondence between the dynamics of the FRET efficiency measured by the phasor trajectory method and the FRET efficiency determined by an intensity ratio as shown in Equation 1.1.

As can be seen from Figure 4.1, the dynamics of the FRET efficiencies do correspond between the two methods of determining the FRET efficiency. We can also see that the phasor trajectory fluctuations correspond to transitions between the three FRET efficiency states determined from bulk measurements, which correspond to the three stable conformations of calmodulin. This demonstrates that the phasor trajectory analysis method is valid and applicable to physical systems, that it is suitable for the analysis of burst lifetime data, and that it allows us to observe the fast conformational transitions of a molecule.

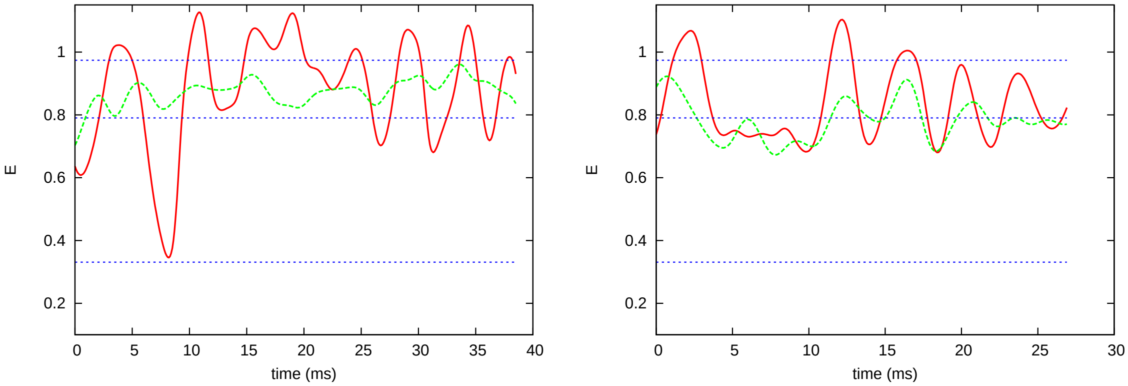

(a) Burst “a” (b) Burst “b”

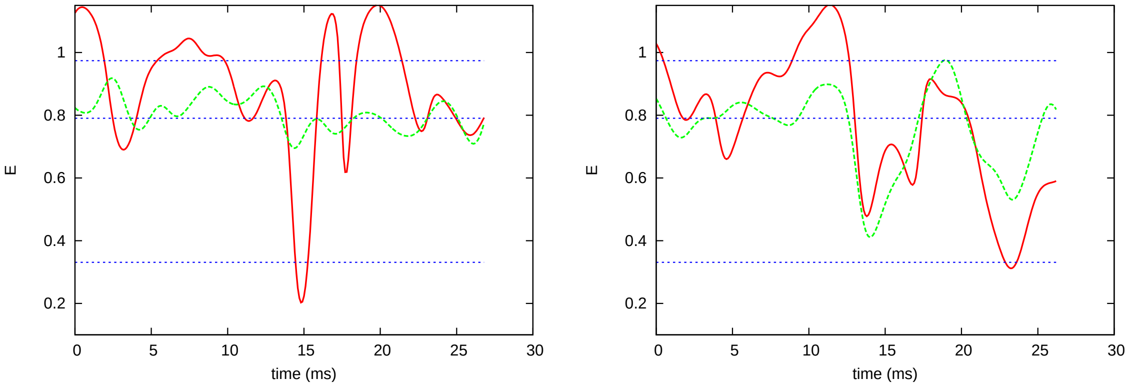

(c) Burst “c” (d) Burst “d”

Figure 4.1: Four single molecule bursts of 1nM calmodulin labeled with Alexa 488 and Texas Red, and diffusing in 40% sucrose with a 5000 cps background. The solid line shows the FRET efficiency calculated from the phasor trajectory, the dashed line shows the FRET efficiency estimated by the intensity ratio method, and the straight dotted lines show the FRET efficiency states for the three conformations of calmodulin as determined from bulk measurements. All bursts were analyzed with an r_s of 2ms. The N values for each point in the these plots are around 30-40 with the two channels combined, yielding a σ_E for the phasor trajectories of around 0.13.

There are several imperfections with these preliminary results which were corrected in subsequent measurements. First, despite using high purity sucrose, there was a small but significant fluorescence background of 2,000 counts per second in the donor channel and 3,000 counts per second in the acceptor channel, which was introduced by the sucrose used in the buffer. This background contributed around 10-15% of the counts during bursts. For the plots in Figure 4.1 this background contribution was subtracted out using the linear properties of phasors (Equations 2.11–2.13). While this is an imperfection in the experimental conditions, the ability to correct for such a problem illustrates a strength of the method, because it indicates that PTA can be performed successfully in the presence of a significant constant background, particularly one with a low modulation. This is an important observation, because this is precisely the condition present in a cellular environment when autofluorescence becomes significant. Therefore, this preliminary measurement indicates that we can reasonably expect success with measurement of a similar probe inside of a cell.

A second imperfection with these preliminary measurements is that the direct contact of the sucrose with calmodulin may alter the very conformational changes we want to observe. This challenges the biological utility of a measurement conducted in the sucrose buffer solution used, and so subsequent measurements were performed by encapsulating in lipid vesicles rather than placing the CaM in direct contact with a viscous agent.

And third, due to space limitations on the APD system at the time of the initial measurements, the measurements were conducted without an optical phase reference for the excitation. In the absence of an optical phase reference, phase drift of the excitation laser on the order of minutes can introduce errors in the resulting position on the phasor plot. For the plots in Figure 4.1, this drift was accounted for by adjusting the reference to compensate for the drift. In all following measurements, the optical phase reference was in place, and the automatic locking of the phase allowed high accuracy without compensation.

4.6 Calmodulin in Lipid Vesicles

For more rigorous experimental conditions, we required a method which slowed the diffusion of CaM through the focal volume while still keeping CaM within a normal aqueous environment. We accomplished this by encapsulating CaM inside of a liposome, which is a lipid vesicle consisting of a spherical lipid bilayer which surrounds an aqueous solution.

We encapsulated CaM inside of 100nm lipid vesicles made of DOPC using the freeze-thaw extrusion process described in [34, 25, 31]. First, DOPC from Avanti Lipids was dried with nitrogen, and placed in a vacuum chamber for two hours to remove the chloroform. Then 500μL solutions were prepared with the buffer described below, DOPC at 5mg/mL, and CaM. The CaM concentration, prior to encapsulation, was set at 32nM to have less than a 1% chance of two CaM molecules in a single vesicle. The solution was then put through five cycles of freezing in -80°C and subsequent thawing. After this, the solution was passed through an extruder with 100nm pores 21 times. A 10cm size-exclusion column was prepared in advance with 10mL of Sepharose 4B beads (Sigma-Aldrich). This was equilibrated with at least 30mL of the buffer being used prior to size-exclusion. After extrusion, the solution was pipetted into the size-exclusion column so that the CaM encapsulated inside of vesicles could be separated from the free CaM.

The size-exclusion process resulted in a number of 10-drop eluates (500μL), which were inspected on the microscope to determine which one contained the highest number of slow bursts. In most cases we found this to occur around eluate 7, where bursts were present every few seconds. The slow diffusion of these 100nm vesicles caused CaM to stay within the PSF for hundreds of milliseconds.

Vesicles were prepared under four buffer conditions. The buffers were prepared at pH 7.4 and contained 100μM NaCl and 40mM sodium phosphate. The first buffer was prepared with 100μM $CaCl_2$, while the second buffer was prepared with 400μM

EGTA to reduce the calcium concentration to nM levels. The third buffer, discussed later, was equivalent to the first buffer, but with HCl added until it reached pH 5. The fourth buffer, also discussed later, was equivalent to the first buffer, but with 320nM of a CaMKII-derived peptide which binds to CaM with high affinity.

4.7 Phasor Trajectories from Vesicles

We acquired data from the vesicles with CaM encapsulated with the 100μM Ca^{2+} buffer for 41 minutes, accumulating 71 independent phasor trajectories which were above a 20 count threshold for 30ms or longer, when r_s was set to 2ms. With the sample encapsulated with the EGTA buffer, due to higher concentrations after column separation we acquired data for 10 minutes and accumulated 4667 phasor trajectories of 30ms or longer using the same r_s. In the EGTA case, the vesicles were observed to aggregate after more than an hour, so only data from shortly after size exclusion is used. This effect was not significant within the time period used for analysis.

4.7.1 Representative Trajectories

Four representative FRET trajectories determined by PTA are shown in Figure 4.2. Figures 4.2a and 4.2b are with a 100μM Ca^{2+} buffer, while Figures 4.2c and 4.2d are with the 400μM EGTA buffer. The analytical uncertainty is shown as a shaded region, and is obtained by applying Equation 3.21 to both the donor and acceptor channels. The straight horizontal dotted lines were determined by a three exponential fit of the lifetime values for a bulk solution of the labeled CaM sample, and are shown to guide the eye in interpreting the states and transitions which are being observed. The middle line is split into two to foreshadow the conclusion that it corresponds to two overlapped states with similar FRET efficiency.

A visual inspection of the data in Figure 4.2 reveals a number of properties. For example, we can observe that the duration for which the molecule persists in a state

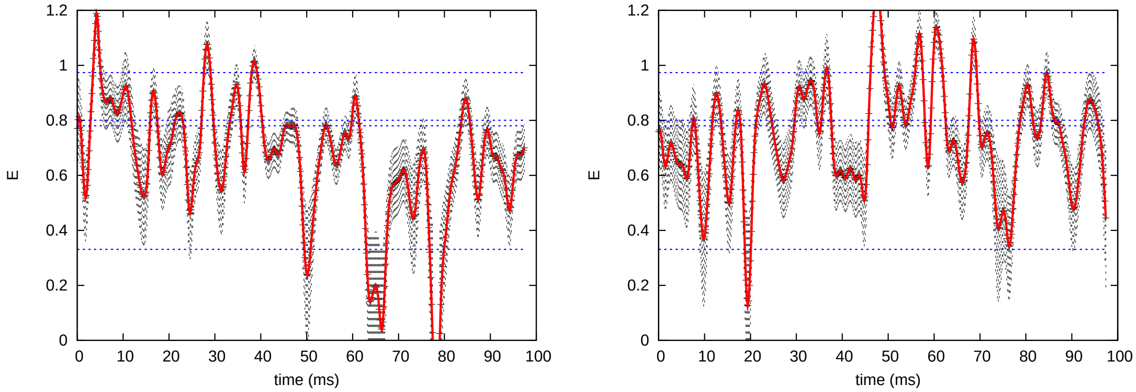

(a) 100μM Ca^{2+}, pH 7.4 (b) 100μM Ca^{2+}, pH 7.4

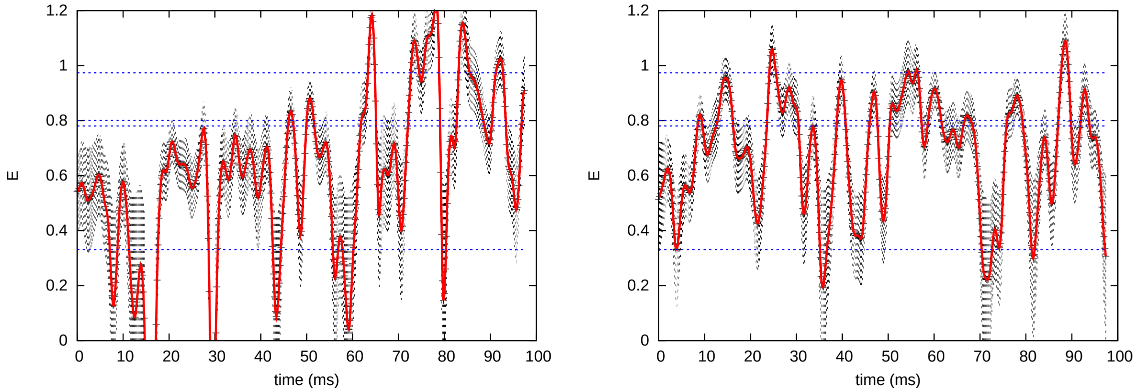

(c) 400μM EGTA, pH 7.4 (d) 400μM EGTA, pH 7.4

Figure 4.2: Four representative FRET trajectories determined by PTA, from four different bursts of CaM in a vesicle, with the analytical uncertainty shown as the shaded region. The straight horizontal dotted lines correspond to the three FRET efficiency values (0.97, 0.79, and 0.33) obtained by a three exponential fit of the lifetime values in a bulk solution. Shown for a buffer with (a, b) 100μM Ca^{2+} at pH 7.4, and (c, d) 400μM EGTA at pH 7.4.

varies, and also, that the molecule appears to enter modes where it favors a distribution of higher or lower FRET states for a period of time. To examine these observations rigorously, we must turn away from inspection of individual trajectories, and instead perform a more quantitative analysis utilizing all of the trajectories.

4.7.2 Moment Analysis

The first thing we desire for a statistical analysis of the properties of the trajectories, is a model-free method for examining and comparing the FRET fluctuations across various samples. Since all of the statistical uncertainties for the system have been characterized with the developments in Chapters 2 and 3, we are equipped with the necessary tools to do a rigorous moment analysis which extracts only the FRET efficiency fluctuations due to the physical changes in the sample.

Since the FRET efficiency can jump to extreme non-physical values with some statistical fluctuations, we will first perform our moment analysis on phase, and then propagate the final result back through to a FRET efficiency value. At every time t, the variance of the phase of the trajectories, σ^2_{traj}, is related to the uncertainty $\sigma_{\phi,PTA}$ given by Equation 3.19, and the phase fluctuation of the sample, Δ_ϕ, according to:

$$\sigma^2_{traj}(t) = \sigma^2_{\phi,PTA}(t) + \Delta^2_\phi(t) \tag{4.1}$$

The phase fluctuation of the sample, given by Δ_ϕ, describes the magnitude of the changes in phase which result from physical changes to the sample, since the statistical fluctuations are accounted for by the other term in the equation. The contribution to the trajectory phase variance at each point in time is calculated from experimental data by:

$$\sigma^2_{traj}(t) = (\phi(t) - \phi_{avg})^2 \tag{4.2}$$

Since these variances add linearly, we can perform a moment analysis on all the bursts from a sample by combining Equations 4.1 and 4.2 with a summation over N_t different points in time:

$$\Delta_{\phi,avg} = \sqrt{\frac{1}{N_t}\left|\sum_{t=0}^{N_t-1} \Delta_{\phi}^2(t)\right|} \tag{4.3}$$

$$= \sqrt{\frac{1}{N_t}\left|\sum_{t=0}^{N_t-1} \left(\phi(t) - \phi_{avg}\right)^2 - \sigma_{\phi,PTA}^2(t)\right|} \tag{4.4}$$

This value can then be converted into a FRET efficiency fluctuation, Δ_E, in a manner analogous to Equations 3.20 and 3.21:

$$\Delta_{\tau_p} = \frac{\Delta_{\phi,avg}}{2\pi f_{ex} \cos^2\left(\phi_{avg}\right)} \tag{4.5}$$

$$\Delta_E = \frac{\Delta_{\tau_p}}{\tau_D} \tag{4.6}$$

Using this analysis we are able to extract a single parameter, Δ_E, which describes the magnitude of FRET efficiency fluctuations which are due to physical changes in the sample. To characterize the limits of this approach, we performed multiple control measurements using 100nM and 200nM fluorescein as a static sample. As shown in Table 4.1, the PTA sample fluctuations in the phase of fluorescein which remain after accounting for the statistical uncertainty are only 1.5°, which is approximately one-tenth the magnitude of the fluctuations observed in the CaM samples. This confirms that this approach has sufficient sensitivity to characterize the fluctuations of the various samples.

If we focus for a moment on the entries of Table 4.1 for the pH 7.4 samples with 400μM EGTA and 100μM Ca^{2+}, we can see that the high calcium sample, with a Δ_E of 0.306, is characterized by substantially increased FRET fluctuations in comparison to the Δ_E of 0.230 in the low calcium case. This analysis shows us in a model-free way that the increase of calcium produces a significant increase in dynamic conformational fluctuations.

	$\Delta_{\phi,avg}$	Δ_E	P
Fluorescein	1.5°	—	—
400μM EGTA, pH 7.4	13.5°	0.230 ± 0.002	0.033
CaMKII-derived Peptide	15.1°	0.265 ± 0.005	0.147
100μM Ca^{2+}, pH 5.0	15.5°	0.271 ± 0.009	0.171
100μM Ca^{2+}, pH 7.4	18.2°	0.306 ± 0.018	0.500

Table 4.1: The average magnitude of fluctuations in phase and FRET efficiency which are attributed to physical changes in the sample, shown for CaM in various environments, and with fluorescein as a static control. The P parameter ranges from 0 to 0.5, and represents the fraction of time the slow domain is in the collapsed state, as given by Equation 4.9. Statistical fluctuations have been subtracted using the equations in Section 4.7.2.

4.7.3 Rise-Fall Histograms

To extract the timescales on which the system returns to the same state, we introduce the rise-fall histogram (RFH) as a model-invariant analysis approach. The RFH is calculated by accumulating a histogram of all the time delays between trajectories passing through the same FRET efficiency value with a slope of the same sign. This approach provides a metric of the timescales of the system periodicities without the introduction of a model.

The RFHs for the 100μM Ca^{2+} and EGTA samples are shown in Figures 4.3a and 4.3b, including a least-squares fit which shows that there are two well-separated timescales of dynamics, one which returns to the same configuration on a 1.1ms timescale, and another which returns to the same configuration on a 6.9ms timescale. Also, the relative amplitudes of the exponentials describing the two processes are a factor of three different between the 100μM Ca^{2+} and EGTA samples. This shows that the slower timescale process occurs much more frequently in the 100μM Ca^{2+} condition.

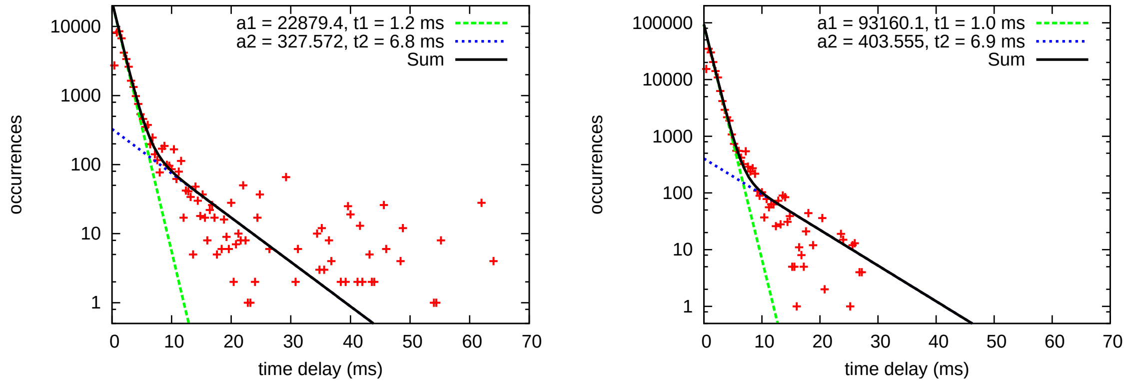

(a) 100μM Ca^{2+}, pH 7.4 (b) 400μM EGTA, pH 7.4

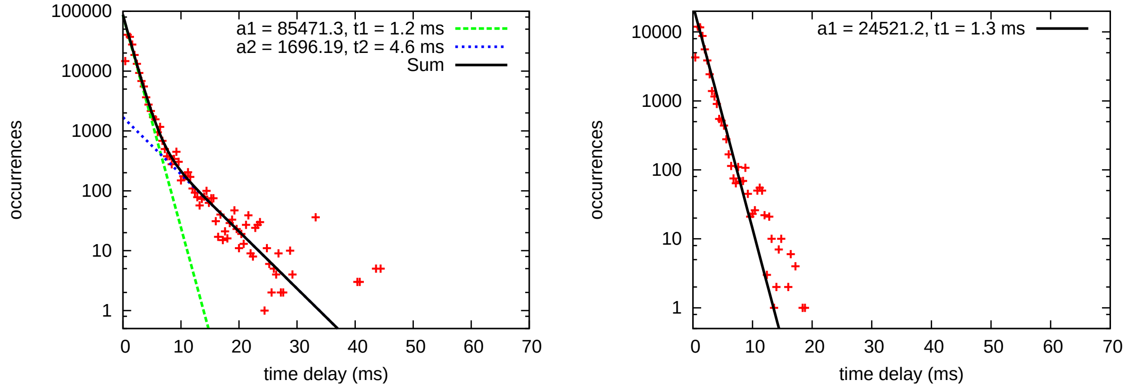

(c) 100μM Ca^{2+}, pH 5.0 (d) CaMKII-derived peptide

Figure 4.3: Logarithmic scale rise-fall histograms (RFHs) showing the time delays between the trajectories passing through the same FRET efficiency value with a slope of the same sign. They show the timescales, given by the least-squares fits of two exponentials, on which the system returns to the same state. The amplitudes and timescales for the short timescale components each have about a 1% error from the fit, while the amplitudes and timescales for the longer timescale components each have about 30% error. Shown for vesicles with (a) 100μM Ca^{2+} at pH 7.4, (b) 400μM EGTA at pH 7.4, (c) 100μM Ca^{2+} at pH 5.0, and (d) 100μM Ca^{2+} at pH 7.4 with 320nM of a CaMKII-derived peptide.

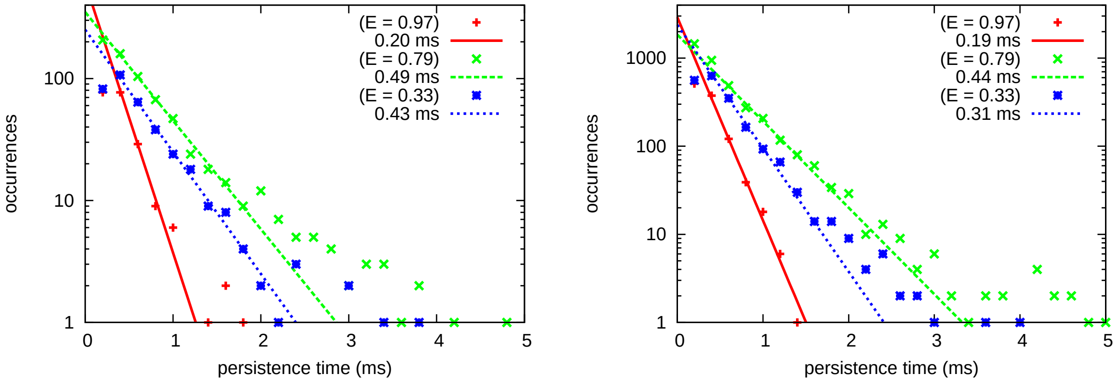

(a) 100μM Ca^{2+}, pH 7.4 (b) 400μM EGTA, pH 7.4

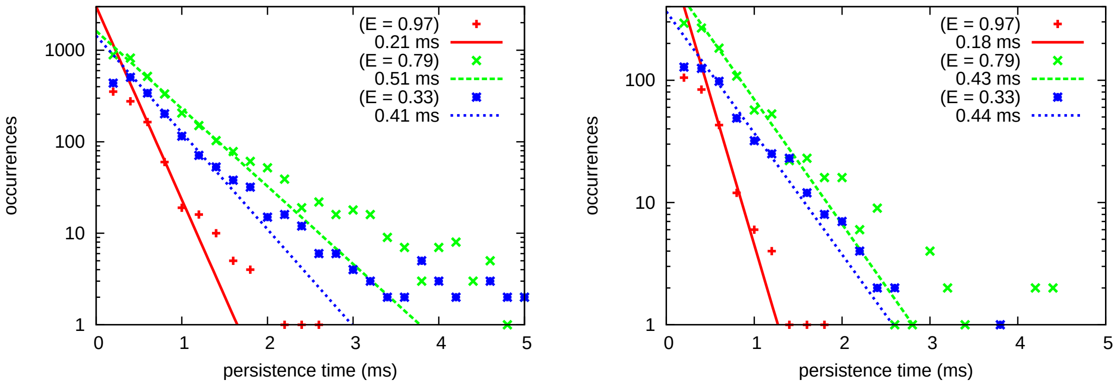

(c) 100μM Ca^{2+}, pH 5.0 (d) CaMKII-derived peptide

Figure 4.4: State persistence histograms generated with $r_s = 0.5$ms, with persistence times determined by fitting the histogram to an exponential decay. These show the duration of each discretized FRET state. Shown for vesicles with (a) 100μM Ca^{2+} at pH 7.4, (b) 400μM EGTA at pH 7.4, (c) 100μM Ca^{2+} at pH 5.0, and (d) 100μM Ca^{2+} at pH 7.4 with 320nM of a CaMKII-derived peptide.

4.7.4 State Persistence Histograms

To obtain a more detailed understanding of the conformational basis for the dynamics observed in the RFH analysis, we can introduce knowledge of the three FRET efficiency states shown in Figure 4.2. By discretizing the trajectories into these three states, which we will call high, mid, and low, we can focus on the temporal behavior of these states. Figure 4.4 shows the persistence times which are obtained from a histogram of the time spent in each state before transitioning to another state. The three FRET efficiencies show persistence times of just under half a millisecond, which indicates that the fastest conformational process transitions on this timescale. While we expect there to be a decrease in measured state persistence times due to uncertainty causing the trajectory to leave the state prematurely, the factor of two difference between these times and the fast component from the RFH is explained in Section 4.8 with the introduction of a conformational model that describes these observations.

4.7.5 Transition Mode Persistence Histograms

In the description of the trajectories shown in Figure 4.2, we noted that the system appears to enter modes where it transitions between high FRET states for a while, or between low FRET states for a while. To examine this observation more rigorously, we calculated transition mode histograms as shown in Figure 4.5, which show the time spent transitioning between the high and mid FRET state, and the time spent transitioning between the mid and low FRET states. In both the 100μM Ca^{2+} and 400μM EGTA cases, the transition modes have a persistence time of around 5ms, with higher calcium significantly decreasing the persistence of the low FRET mode, and increasing the persistence of the high FRET mode. This reveals that there is a slower timescale process, corresponding to the slow timescale periodicity of the RFH, which manifests as a shift in FRET efficiency between low and high modes, while the

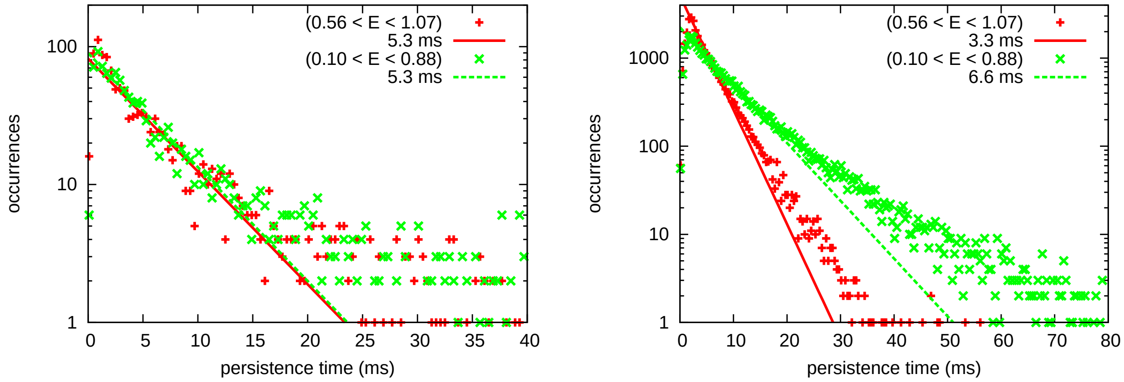

(a) 100μM Ca^{2+}, pH 7.4 (b) 400μM EGTA, pH 7.4

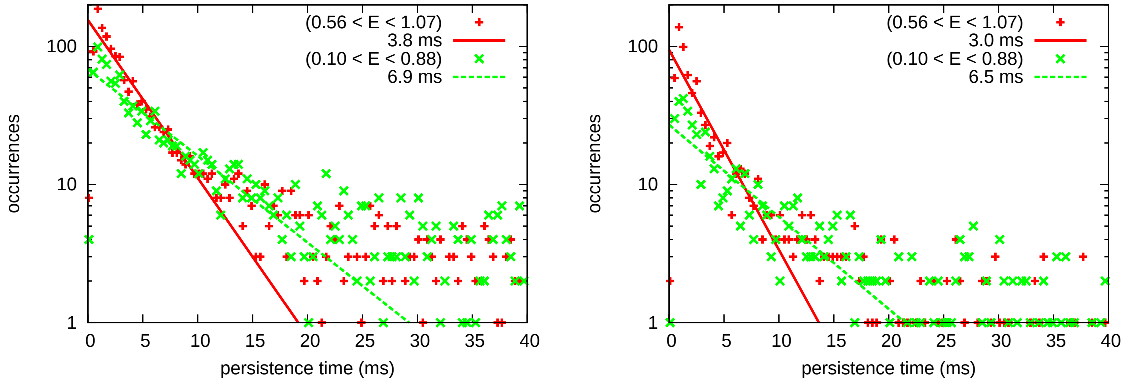

(c) 100μM Ca^{2+}, pH 5.0 (d) CaMKII-derived peptide

Figure 4.5: Transition mode persistence histograms, generated with $r_s = 2$ms. These show the duration of the high-mid (+ and solid line) and mid-low (x and dashed line) transition patterns. Shown for vesicles with (a) 100μM Ca^{2+} at pH 7.4, (b) 400μM EGTA at pH 7.4, (c) 100μM Ca^{2+} at pH 5.0, and (d) 100μM Ca^{2+} at pH 7.4 with 320nM of a CaMKII-derived peptide.

faster timescale process operates in addition to this slower offset. This also reveals that the shift in state distributions with calcium concentration observed by [41] can be explained in terms of a calcium dependent shift in the time spent in the two states of this slower process.

4.8 Conformational Interpretation

It's well known from NMR studies that CaM has two domains, each of which has a tendency to bind or unbind two Ca^{2+} ions at a time [3, 43]. If we combine this observation with the FRET dynamics described above, then we can propose a conformational interpretation for the trajectories observed, as shown schematically in Figure 4.6. We attribute the two independent timescales observed to the two domains of CaM, with differently sized energy barriers resulting in a fast domain and a slow domain. Within this interpretation, the binding or unbinding of 2 Ca^{2+} ions with the fast domain causes the fast timescale state transitions which are observed in both the high transition mode and low transition mode. Then the process of binding or unbinding of 2 Ca^{2+} ions with the slow domain is responsible for the slower timescale transitions between the two transition modes. Note that the middle FRET state in this model is actually produced by two distinct FRET states which are indistinguishable with the precision available. They can, however, be distinguished by examining the dynamic behavior of the system, as was done above.

By examining the model shown in Figure 4.6, we can compare the numerical results obtained from Figures 4.3, 4.4, and 4.5. Since the RFH shows the delay time before the trajectory returns to its previous position with the same slope, we can note that the state persistence time (0.4ms) must be doubled to compare with the fast component of the RFH time (1.1ms). Similarly, with the model shown, the persistence time of the slow domain (5.3ms) plus the fast component of the RFH (1.1ms) should correspond to the slow component of the RFH time (6.9ms). This high degree of correspondence provides validation for the model, and shows that information about the system dynamics can be obtained with a model invariant approach (Figure 4.3) or in more detail by applying known information.

With a conformational interpretation for the dynamics which were observed, we can formulate a schematic representation of the four molecular states which correspond to the observations, and we can map the measured timescales to the timescales of the state transitions for the model, as shown in Figure 4.7. In this four-state model, each domain has two configurations, leading to a total of four possible states. The two transitions which change the conformation of the fast domain occur on a half millisecond timescale, while the two transitions which change the conformation of the slow domain occur on a five millisecond timescale. Not shown on the schematic is the calcium dependence of these transitions, where in particular the slow domain has an increased preference for the two states in which it is in the expanded conformation (low FRET) when the calcium concentration is low.

4.9 Moment Analysis of Domains

If we introduce model information to the moment analysis from Section 4.7.2, then we can extract significantly more information about the individual domains. For example, it was shown in Sections 4.7.4 and 4.7.5 that the FRET fluctuations in the 100μM Ca^{2+}, pH 7.4 case correspond to two independent domains with fluctuations of similar magnitude fluctuating equally between the available states. Using this information, we can utilize the linearity of variance to separate the two fluctuating domains:

$$\Delta_E^2 = \Delta_{E,slow}^2 + \Delta_{E,fast}^2 \tag{4.7}$$

We can conclude that for the 100μM Ca^{2+}, pH 7.4 environment, with a Δ_E of 0.306, each domain has a magnitude of $\Delta_{E,one} = 0.306/\sqrt{2} = 0.216$. It was also

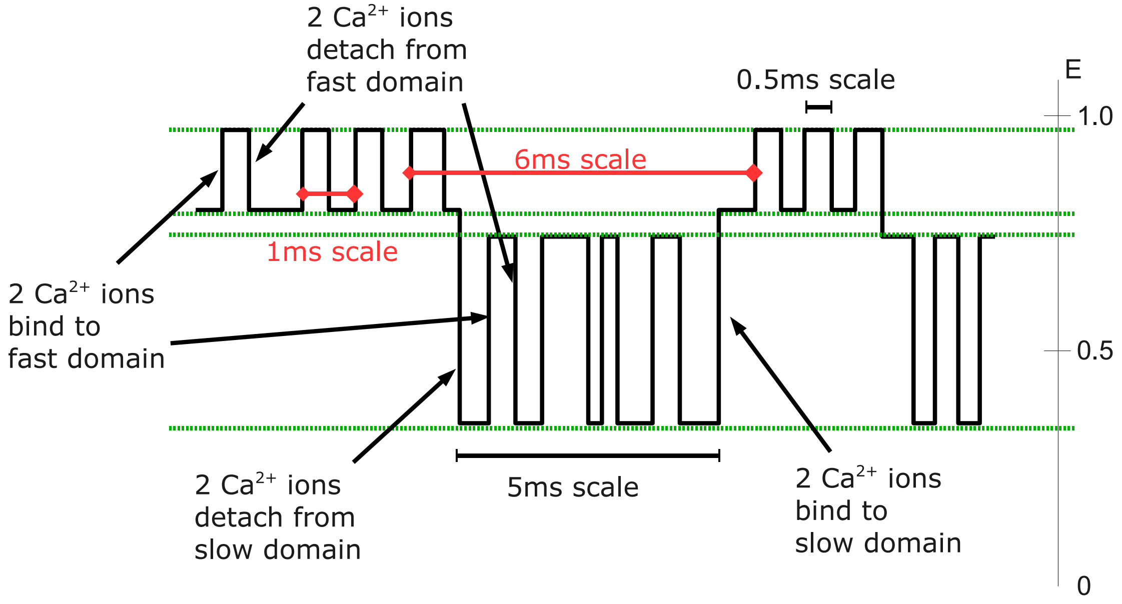

Figure 4.6: A schematic of the conformational interpretation of the dynamic FRET behavior observed with CaM. The 0.5ms scale corresponds to the state persistence observed in Figure 4.4, the 5ms scale corresponds to the transition mode persistence observed in Figure 4.5, and the 1ms and 6ms scales correspond to the values from the RFHs in Figure 4.3. Shown for the 100μM Ca^{2+}, pH 7.4 environment.

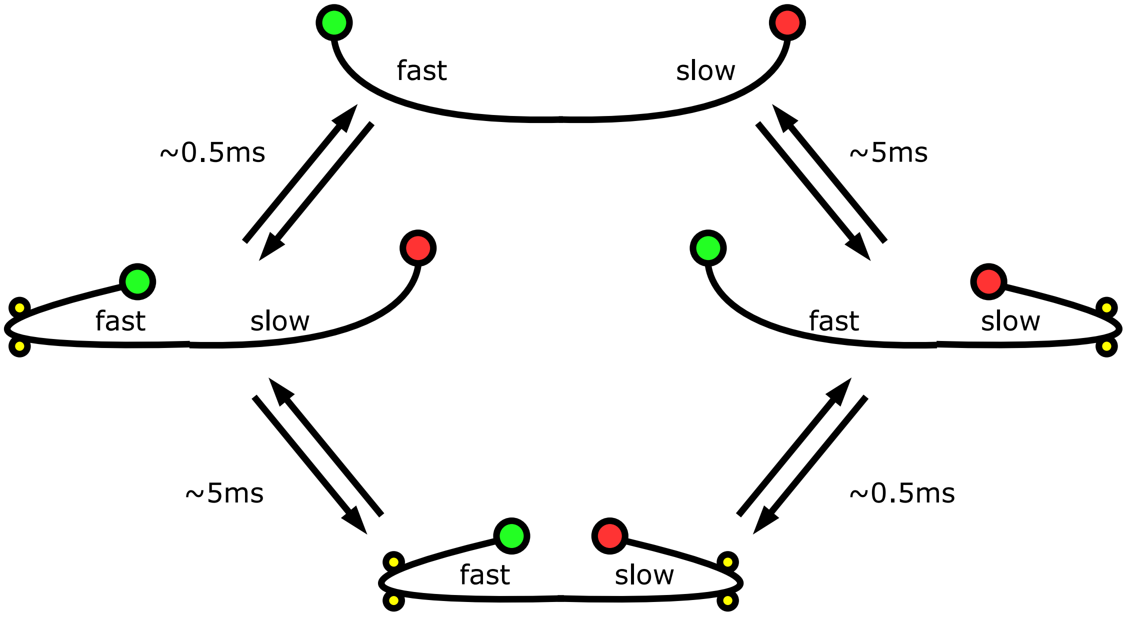

Figure 4.7: A schematic of the four state CaM system, showing the possible conformations and the timescales of transitions between these four conformations. Shown for the 100μM Ca^{2+}, pH 7.4 environment.

shown in Section 4.7.3 that in each of the environments, the fast domain is always fluctuating. We can then characterize the distribution of states for the slow domain by defining a variable P as the fraction of time (ranging from 0 to 0.5) that the slow domain spends in its less likely state. Then a relationship between $\Delta_{E,slow}$ and P can be established by using the formula for the variance of a two-state system:

$$\Delta^2_{E,slow} = D^2 P\,(1-P) \tag{4.8}$$

where D, the separation of the two states, can be approximated by inserting the values for 100μM Ca^{2+}, pH 7.4, yielding a value of $D = 4\Delta_{E,one}$.

By combining Equations 4.7 and 4.8, we obtain an expression for P given by:

$$P = \frac{1-\sqrt{2-\left(\frac{\Delta_E}{\Delta_{E,one}}\right)^2}}{2} \tag{4.9}$$

We now have an expression which relates Δ_E, the fluctuation of FRET efficiency due to physical changes in the sample, to P, the fraction of time that the slow domain spends in its less likely state. By examining the range of P values in Table 4.1, we can quantitatively see the range of conformational state distributions which are represented by the various environments which were measured. For example, in the EGTA case with low calcium levels, the moment analysis shows that the slow domain is rarely in the calcium-bound state.

4.10 Low pH Buffer

Yao et al. used lifetime changes in the intrinsic tyrosine fluorescence of CaM to show that under pH 5.0 conditions, calmodulin enters a less compact state similar to its conformation under low-calcium conditions [46]. Following this line of consideration, we prepared a 100μM Ca^{2+} buffer at pH 5.0, and repeated the CaM/vesicle experiment under this condition. We obtained 140 trajectories which remained above 20 counts for over 30ms when using a resampling scale of 2ms.

As listed in Table 4.1, the moment analysis of the pH 5.0 sample showed a Δ_E of 0.255, yielding a larger conformational fluctuation than the EGTA case, but smaller than in the 100μM Ca^{2+} pH 7.4 case. The P value for the pH 5.0 measurement was 0.147, confirming that the slow domain was most often in the expanded conformation, indicating the calcium-free state. The relative amplitude of the two RFH components shown in Figure 4.3c are comparable to the pH 7.4 case, although the timescale of the longer component is shortened slightly.

From the state persistence histogram in Figure 4.4c we can see that, as shown with the RFH analysis, the fast component remains unchanged. However, with the transition mode persistence histogram from Figure 4.5c, we can see that the slow timescale behavior is similar to the low calcium EGTA condition of Figure 4.5b. This indicates that the low pH condition produces a preference for the expanded conformation in the slow domain, similar to that obtained with a low calcium environment.

In contrast to [46] and the results obtained here, in [41] they observed a more compact state at pH 5.0, but this may have been due to the high level of magnesium in their buffer. Magnesium is known to interfere with the calcium binding in calmodulin [29] at the 1mM level used in their buffer, and this may result in alternate behavior at low pH. Since the interaction between magnesium and calcium at calmodulin's binding sites is of physiological significance, this difference in behavior may be worth investigating in future experiments.

4.11 Conformational Dynamics with the CaMKII-Derived Peptide

Ca^{2+}/calmodulin dependent protein kinase II (CaMKII) is a multifunctional protein kinase which phosphorylates a wide variety of proteins when activated by Ca^{2+} and CaM. It is the mechanism by which CaM affects a wide variety of processes in metabolism, neurotransmitter synthesis and release, ion channels, and cytoskeletal function [23]. In 1998, Waxham et al. showed that when CaM binds to CaMKII, it becomes trapped by a sequence of conformational changes in CaMKII [45]. To investigate the effect this trapping process has on the conformational dynamics of CaM, we obtained a sample of the CaMKII-derived peptide, CaMKII(292-314) KFNARRKLKGAILTTMLATRNFS, which was donated by M. Neal Waxham. This peptide contains the sequence to which CaM binds when trapped, and thus emulates the most-bound state of CaM to CaMKII [45]. We performed the CaM/vesicle experiment with a 100μM Ca^{2+} pH 7.4 buffer containing 320nM of the CaMKII(292-314) peptide, and obtained 32 trajectories which remained above 20 counts for over 30ms when using a resampling scale of 2ms.

The RFH plot in Figure 4.3d shows an even more pronounced change in conformational dynamics from binding to the peptide. In it, the slower timescale is nearly completely suppressed, leaving only the faster 1.3ms timescale, which corresponds to the fluctuation of the fast domain. This indicates that the fluctuation of the slow domain is what is significantly reduced in magnitude, while the fast domain continues to fluctuate freely.

The magnitude of fluctuation obtained from the moment analysis and shown in Table 4.1 would seem to indicate that the slow domain fluctuates more frequently than in the EGTA case. However, that interpretation cannot be made using only the moment analysis results. The moment analysis is invariant with respect to the time sequence of values measured, and as the values in Table 4.1 are from the analysis of all bursts, this only reveals the distribution of FRET efficiency values obtained from all bursts. The RFH, in comparison, directly examines the behavior of the time sequence. In combination, the RFH shows that the slow domain's fluctuation is suppressed, while the moment analysis says that the slow domain still exists in a distribution of conformations. This leads to the conclusion that the slow domain is largely locked down, with any fluctuations on a timescale longer than the durations of observed bursts, but that it is present in more than one state.

In the state persistence histogram in Figure 4.4d, the fluctuation of the fast domain is shown to be identical to the other buffer conditions, in agreement with the observation from the RFH. If we also force the data to fit the transition mode model, which selectively analyzes only those bursts which do happen to complete a full fluctuation cycle of the slow domain (since these are the only ones with timing information on the slow domain), then we obtain Figure 4.5d. The magnitudes are low in this figure, since as shown in the RFH, few bursts complete this cycle. From this figure we can see a preference for remaining in the low FRET transition mode longer, which indicates that the more stable bound conformation is one in which the two FRET pairs are at a similar distance to when the slow domain is in the expanded state. However, because it is also bound to a peptide which is known to alter the conformation of CaM [45], we cannot directly conclude that these conformations are exactly equivalent using the single parameter obtained from a FRET measurement.

We can therefore note three important conclusions from this measurement. First we can note that the fluctuations of the slow domain are significantly suppressed, indicating that it is constrained by the CaMKII binding process. Second, we can note that the slow domain is locked down in more than one conformation. And third, we can note that the fluctuations of the fast domain continue unhindered while bound to the peptide, which indicates that they may continue as an equivalently dynamic process while bound to CaMKII under physiological conditions.

4.12 Discussion

The phasor trajectory analysis of fluorescence lifetime changes due to FRET allows us to observe protein conformational dynamics under single molecule conditions and on millisecond timescales. Using this approach, we were able to characterize the fluctuations and temporal behavior of the conformational transitions of calmodulin, and we were able to use the time information to associate these transitions with the four state model which describes the conformational dynamics of CaM. We also used these techniques to investigate the changes to this dynamic behavior in the presence of low and high calcium, and at different pH. We were also able to show that upon binding to a CaMKII-derived peptide, the dynamic behavior of one of CaM's domains is significantly suppressed, while the faster domain continues to fluctuate.

By performing a moment analysis which used the analytical uncertainty equations to remove the statistical fluctuations at each point in time, we were able to obtain a FRET fluctuation parameter which describes the distribution of FRET efficiencies which resulted from conformational changes. Using fluorescein as a static control we were able to characterize the limits of this analysis, and showed that the CaM results are well above this limit. This analysis approach showed quantitatively that the magnitude of FRET fluctuation has a strong dependence on calcium concentration, where the high calcium condition showed a fluctuation magnitude approximately equivalent to two domains fluctuating relative to one domain fluctuating in the low calcium condition. This corresponds quite well with the amplitudes obtained from the rise-fall histograms for the two conditions, where it was shown that the low calcium condition experiences less than a third of the fluctuation in the slow domain as the high calcium condition, while both experience similar fluctuation in the fast domain.

In a microfluidic mixer study by Park et al., they found that upon rapid addition of calcium, CaM reached its first equilibrium after 0.5ms, and a second equilibrium after 20ms [35]. These timescales correspond well to the timescales observed here for the binding processes in the fast and slow domains. As there was a calcium concentration dependence observed here for the transition to the collapsed calcium-bound state of the slow domain, it is conceivable that the longer timescale observed in the microfluidic mixer study can be attributed to the local calcium concentration. It may be insightful to examine the dynamics of this domain under a wider range of calcium concentration conditions in future work.

An assortment of NMR and stopped flow studies have examined the unbinding of Ca^{2+} from CaM, and have observed timescales ranging from around 0.7-2ms as a fast unbinding process, and around 20-100ms as a slow unbinding process [2, 3]. Teleman et al. conducted an NMR binding kinetics study using two tryptic fragments corresponding to the N-terminal half of CaM, with Ca^{2+} binding sites I and II, and the C-terminal half of CaM, with binding sites III and IV [43]. They were able to assign the N-terminus as the domain which exhibited fast unbinding, and they were also able to assign the C-terminus as the domain which exhibited slow unbinding.

Exploiting this information, and extending it to include the dynamics shown here, we can therefore assign the fast fluctuating domain as the N-terminus, and the slow fluctuating domain as the C-terminus. Because we have characterized the full time sequence of the conformational transitions, and thus know that the same domain experiences fast binding as fast unbinding, we can extend the previous understanding to include the information that the N-terminus also experiences fast binding, while the C-terminus also experiences slow binding.

In the intensity-FRET based BIFL study done in [41], it was noted that the mid-FRET state shifts its average FRET value based on calcium concentration, which hints that it actually corresponds to two overlapped states with slightly different FRET values, but that they are too close to be resolved. This corresponds to the observations made here, where the two states were also too close to resolve. However, with the additional time information, we were able to distinguish the two FRET states (corresponding to the left and right state in Figure 4.7) by their dynamic behavior, since the left state in that figure is more likely to transition to the top state, while the right state is more likely to transition to the bottom state.

Drum et al. studied the anthrax exotoxin called oedema factor (EF), which is activated by the CaM naturally present in the infected host, and discovered that when CaM binds with EF, it has only two Ca^{2+} ions bound to the C-terminus, and no Ca^{2+} ions bound to the N-terminus [15]. This highlights that the intermediate states with partial calcium binding have significant physiological impact for the activation of certain targets.

To discern the impact of intermediate states of CaM's interaction with CaMKII, Shifman et al. conducted a study of the binding of CaM to CaMKII using CaM mutants which disabled the Ca^{2+} binding capability of one terminus locking it in the calcium-free conformation, with one mutant having the N-terminus disabled, and another having the C-terminus disabled. They were able to observe that CaM with either single terminus locked in the calcium-unbound state was still able to bind to CaMKII and activate it, but that the mutant with the N-terminus locked in the unbound state (and C-terminus still active) was far more effective at doing this than the mutant with the C-terminus locked in the unbound state [40]. This indicates that the conformational change which happens upon calcium binding to the C-terminus is more critical to the binding of CaM to CaMKII. In the analysis presented here, we observed that the C-terminus, corresponding to the slow domain, was locked with a significant suppression of its dynamics upon binding to the CaMKII-derived peptide. Combined, these results show that the C-terminus is the more active agent in the binding to CaMKII, and that the transitions of the C-terminus are more significantly affected by the binding to CaMKII. This illustrates a system of bidirectional influence between the conformation of the C-terminus and CaMKII.

In the environments tested here, CaM does not appear to behave as a protein which changes to another static conformation in the presence of a calcium concentration change, but instead as a highly dynamic molecule with complicated temporal behavior governed by the two different domains. It was also shown that the freedom of motion of the slower domain is significantly suppressed when bound to a CaMKII-derived peptide which mimics the binding of CaMKII, but that the faster domain continued to fluctuate freely. This indicates that CaM may experience a similar alteration of its dynamic behavior when bound to CaMKII as part of its physiological function within a cellular environment. This alteration in dynamic behavior may be related to the process by which CaMKII and its targets are phosphorylated, and thus may be a critical step in the regulation of CaM as a signaling protein. The alteration of CaM's dynamic behavior may also be related to the process of unbinding from its targets such as CaMKII, which is a necessary step for CaM to bind with competing targets.

Using stopped-flow techniques, Brown et al. examined the dissociation of CaM from target peptides after calcium removal. They determined that the dissociation rates were not determined directly by peptide affinities, but instead were governed by a kinetic pathway in which CaM first transitions into an intermediate state with calcium only bound to the C-terminus [7]. By combining this information with the results obtained here, we can present an answer to the first question posed in Section 4.2 regarding the mechanism by which CaM switches binding targets when there is very little free CaM. With the data described in Section 4.11 we showed that when CaM is bound with high affinity to a CaMKII-derived peptide, the N-terminus continues to undergo dynamic behavior in which its Ca^{2+} ions unbind roughly a thousand times a second. Therefore, even while bound to this peptide, it appears that CaM frequently samples the kinetic pathway which has been shown to be the mechanism for dissociation. This dynamic behavior may be a critical part of the mechanism which allows CaM to rapidly change binding targets in response to changes in calcium concentration.

The question posed in Section 4.2 regarding the alteration of CaM's dynamic behavior by the binding target can also be addressed using the data presented here. As was shown in Section 4.11, the dynamic behavior of the C-terminus was significantly suppressed, indicating that it is held locked in place by the CaMKII-derived peptide. In [7] it was shown that CaM's peptide dissociation process primarily follows two paths. One pathway was the dissociation of the peptide after the unbinding of the Ca^{2+} ions from the N-terminus, but prior to the unbinding Ca^{2+} ions on the C-terminus. The second pathway was the dissociation of all four Ca^{2+} ions, followed by the dissociation of the peptide. Therefore, the mutual interaction seen here with the peptide increasing the stability of the C-terminus is expected to have an impact on the second of these two kinetic pathways. A complete understanding of this process can only be obtained by considering the system in conjunction, as the components have a complex mutually interacting behavior.

4.13 Conclusion

The results obtained with PTA and the assortment of analysis techniques presented here provided valuable insight into the complicated dynamic behavior of CaM and its interaction with calcium, environmental conditions, and its binding targets. Examined directly, PTA produced FRET trajectories which allowed the direct visual inspection of the FRET efficiency changes which CaM experienced. The moment analysis techniques provided quantitative information about the distribution of states observed, while the RFH analysis provided a model-free analysis of the temporal characteristics of CaM's dynamic behavior. The state persistence histograms and transition-mode persistence histograms allowed the introduction of known state information to extract more detailed information about the time sequences of the observed FRET states, which allowed the characterization of a specific conformational description of the FRET transitions. When considered as an aggregate whole, the combination of these analysis approaches provided a detailed description of the dynamic behavior of CaM, and showed that a wide-assortment of information can be obtained from a direct observation of the conformational dynamics of a protein under single-molecule conditions.

The APD-based setup in conjunction with a DFD lifetime approach proved useful for the attainment of adequately high count rates to perform this analysis. With further improvements in count rate, such as by increasing the excitation intensity, quantum yield of the fluorophore, or collection efficiency, PTA can be extended to shorter timescales or higher FRET efficiency precision. Precision improves by the square root of the number of counts, while the timescale which can be observed scales inversely with the number of counts. By choosing a resampling scale, one makes a trade-off between the precision obtained and the timescale which can be observed. However, the PTA approach allows one to obtain both conditions with the same set of data by using multiple resampling scales during analysis.

PTA provides the ability to observe FRET fluctuations on the millisecond timescale under single-molecule conditions, using the combined lifetime information from both the donor and acceptor channels. With the associated analysis techniques presented here, the tools are provided to examine a wide assortment of additional questions regarding the dynamic behavior of fast-fluctuating proteins. PTA also allows the observation of these fluctuations with a high rejection of background counts and insensitivity to imperfections in the intensity profiles. Because of these features and the capabilities demonstrated here, phasor trajectory analysis may be valuable for studying dynamics in further single-molecule studies.

Chapter 5

Conclusion

5.1 Summary

The combination of digital frequency domain (DFD) fluorescence lifetime acquisition with phasor trajectory analysis (PTA) was used for a detailed single molecule study of the conformational dynamics of calmodulin (CaM) in the presence of its binding partners. To achieve this goal, a comprehensive DFD theory was developed, leading to the development of optimal DFD lifetime hardware, and universal phasor uncertainty equations were derived, which apply to data from any photon counting system which is analyzed with a phasor analysis.

To enable the study of conformational dynamics under the low-count conditions present in a single molecule experiment, phasor analysis was extended to the PTA approach, and the phasor uncertainty equations were extended to PTA uncertainty equations. Analysis of these equations showed the experimental conditions which were required for single molecule study, and allowed accurate theoretical prediction of the measurements which could be made.

These developments were then applied to the study of the conformational dynamics of CaM using a CaM sample which was labeled with a pair of fluorophores which experience FRET. The labeled CaM sample was encapsulated inside of lipid vesicles under various buffer conditions which varied the calcium concentration, the pH, and the presence of a peptide derived from the CaM binding site of CaMKII. FRET trajectories were obtained with PTA, which allowed the direct observation of the conformational dynamics under the given conditions.

Several new analysis techniques were also developed which allowed the quantitative determination of the changes to dynamic behavior which occurred with differing experimental conditions. A moment analysis was developed which utilized the uncertainty equations to remove statistical fluctuations, leaving only the variation which resulted from physical fluctuations and the distribution of these states. A rise-fall histogram analysis was developed which provided a model-free way of examining the timescales of dynamic behavior present in the FRET trajectories. In addition, information about the known stable FRET states was used to obtain persistence histograms. These analyses were then used to develop a detailed conformational model describing the behavior of CaM in the presence of various molecular interactions with its binding partners.

5.2 Future Prospects

There are a significant number of future prospects for this work. The developed hardware described in Chapter 2 is a general purpose lifetime acquisition system which supports lifetime imaging, intensity imaging, and a wide variety of point or image correlation techniques. The DFD theory and phasor uncertainty equations presented there are sufficiently general that they can be used to guide development of subsequent generations of DFD hardware, such as hardware which can obtain large numbers of harmonics in parallel, or hardware supporting lifetime acquisition on large numbers of channels.

PTA has been demonstrated here as a technique for the observation of single molecule conformational dynamics, but is in principle a much more general tool which can be used for the observation of lifetime changes of any cause and on any timescale with sufficient counts. This could even be used in ensemble measurements to observe dynamic changes of the fluorophores in a region due to signaling, physical motion, or chemical processes.

One specific area PTA could be extended as a technique is by the inclusion of additional wavelength regions, or with full spectral analysis. For the experiment presented in Chapter 4 there was a 110nm wavelength gap between the bandpass filters for the donor and acceptor channels, in which many photons fell. These were excluded to make bleedthrough easier to deal with, but this resulted in a significant loss of photons. As shown in Chapter 3, both donor and acceptor photons contain lifetime information for the donor, and therefore, the photons in this gap also do. With spectral information for the donor and acceptor fluorophores and a spectral lifetime system, PTA can be extended to include the full range of available photons, resulting in higher precision, the ability to extend to smaller timescales, and superior background exclusion.

Hidden Markov Modeling (HMM) has shown promise as a technique for extracting conformational states and transition probabilities from an intensity FRET trajectory [32], and it should be possible to use with a phasor sequence as well. However, there are some theoretical complications involved in a combination of these techniques, since the moving average used here contradicts the fundamental Markov assumption of future states depending only on the present state. Therefore, combining these techniques requires either an analysis which calculates directly on the sequence of phase bin numbers, sacrificing many of the advantages of background rejection, or an analysis which uses time bins without a moving average, which would likely require higher counts to observe the same dynamics.

One prospect for observing molecules for longer time intervals may be by combining the techniques presented here with 3D particle tracking done by orbital scanning [28]. With sufficient signal-to-noise, this would permit the tracking of a single molecule for time periods limited only by bleaching. Another approach which offers the possibility of parallel observation of the lifetime dynamics of multiple molecules with spatial resolution is in the development of high quality lifetime imaging detectors [33]. This may have particular value for cellular applications of these techniques, since macromolecules are likely to exhibit different behavior in different regions of a cell.

There are also a number of future prospects for the application presented in Chapter 4. A straightforward extension would be to examine CaM's behavior in the presence of other binding targets to determine if the binding behavior differs from that observed here with the CaMKII-derived peptide. Differences in conformational behavior when bound to different binding targets targets may be an integral part of the mechanism of competitive binding in the presence of calcium concentration changes.

Another useful extension would be the application of PTA to the study of CaM's behavior within a cell. For example, it may be possible to directly address questions about the free CaM in a cell by examining the conformational dynamics. It may also be possible to use a moment analysis of individual bursts to resolve subpopulations, and by doing so distinguish free CaM from bound CaM. If individual CaM molecules can be observed for sufficient duration within a cell, some time sequences may show transitions between free and bound, which would reveal information about the conformational processes involved.

A new difficulty which arises when extending this technique to a cell is introduced by aggregation, since some of CaM's binding targets bind multiple CaMs at once. For example, CaMKII can bind up to 12 CaM molecules at a time. If multiple labeled CaM molecules are present in the focal volume simultaneously, then the measured phasor will be an average of their individual phasors, smearing out the desired dynamics. One approach to resolving this problem would be to keep the concentration of labeled CaM sufficiently low that aggregates with two or more labeled CaM are unlikely. Under this concentration, the rare labeled CaM molecules could still be observed as single molecules.

More generally, these techniques could also be applied directly to a wider assortment of macromolecules with dynamic behavior, such as ribosomes, syntaxin, or various enzymes.

5.3 Conclusion

DFD lifetime acquisition provides fluorescence lifetime information with precision comparable to the leading techniques in the field, yet with an inexpensive approach which is more easily scaled to multiple channels. Also, the phasor uncertainty equations which were developed allow a detailed theoretical assessment of optimal system parameters, and provide a rigorous knowledge of the uncertainty of a measured lifetime value.

The extension of phasor analysis to PTA provides a powerful capability for the observation of dynamic lifetime changes, and in particular, for constructing FRET trajectories which merge lifetime information from both donor and acceptor emission. This information was used with new analysis techniques such as the rise-fall histograms, moment analysis, and persistence histograms to develop a detailed picture of the molecular basis for the conformational dynamics of CaM. The detailed dynamics provided by this single molecule approach were used to answer questions about the specific conformational transitions CaM experiences when interacting with binding partners.

The combination of these developments provides a valuable new approach to addressing physiologically important questions by the measurement of fluorescence lifetime changes which result from single molecule reactions.

References

[1] Michael W Allen, Ramona J Bieber Urbauer, Asma Zaidi, Todd D Williams, Jeffrey L Urbauer, and Carey K Johnson. Fluorescence labeling, purification, and immobilization of a double cysteine mutant calmodulin fusion protein for single-molecule experiments. *Analytical Biochemistry*, 325:273–284, 2004.

[2] Thomas Andersson, Torbjörn Drakenberg, Sture Forsén, and Eva Thulin. Characterization of the Ca^{2+} binding sites of calmodulin from bovine testis using ^{43}Ca and ^{113}Cd NMR. *Eur. J. Biochem.*, 126:501–505, 1982.

[3] Peter Bayley, Peter Ahlström, Stephen R Martin, and Sture Forsen. The kinetics of calcium binding to calmodulin: Quin 2 and ANS stopped-flow fluorescence studies. *Biochem & Biophys Res Comm*, 120:185–191, 1984.

[4] M N Berberan-Santos. The time dependence of rate coefficients and fluorescence anisotropy for non-delta production. *Journal of Luminescence*, 50:83–87, 1991.

[5] M N Berberan-Santos and J M G Martinho. Kinetics of sequential energy-transfer processes. *J. Phys. Chem.*, 94:5847–5849, 1990.

[6] J B Birks. Energy transfer in organic systems: VI. Fluorescence response functions and scintillation pulse shapes. *J. Phys. B*, 1:946–957, 1968.

[7] Susan E Brown, Stephen R Martin, and Peter M Bayley. Kinetic control of the dissociation pathway of calmodulin-peptide complexes. *The Journal of Biological Chemistry*, 272(6):3389–3397, 1997.

[8] Andrew Catalano and Danton H O'Day. Calmodulin-binding proteins in the model organism Dictyostelium: A complete & critical review. *Cellular Signalling*, 20:277–291, 2008.

[9] A H Clayton, Q S Hanley, and P J Verveer. Graphical representation and multicomponent analysis of single-frequency fluorescence lifetime imaging microscopy data. *J Microsc*, 213(Pt1):1–5, 2004.

[10] R Clegg, B Feddersen, E Gratton, and T Jovin. *Time-Resolved Laser Spectroscopy in Biochemistry III*, pages 448–460. SPIE, 1992.

[11] Robert M Clegg. *Fluorescence Imaging Spectroscopy and Microscopy*, chapter 7, pages 179–252. John Wiley & Sons, Inc., 1996.

[12] Ryan A Colyer, Claudia Lee, and Enrico Gratton. A novel fluorescence lifetime imaging system that optimizes photon efficiency. *Microscopy Research and Technique*, 71:201–213, 2008.

[13] Ashok A. Deniz, Maxime Dahan, Jocelyn R Grunwell, Taekjip Ha, Ann E Faulhaber, Daniel S Chemla, Shimon Weiss, and Peter G Schultz. Single-pair fluorescence resonance energy transfer on freely diffusing molecules: Observation of Förster distance dependence and subpopulations. *PNAS*, 96:3670–3675, 1999.

[14] Michelle A Digman, Valeria R Caiolfa, Moreno Zamai, and Enrico Gratton. The phasor approach to fluorescence lifetime imaging analysis. *Biophys J*, 94(2):L14–16, 2008.

[15] Chester L Drum, Shui-Zhong Yan, Joel Bard, Yue-Quan Shen, Dan Lu, Sandriyana Soelaiman, Zenon Grabarek, Andrew Bohm, and Wei-Jen Tang. Structural basis for the activation of anthrax adenylyl cyclase exotoxin by calmodulin. *Nature*, 415:396–402, 2002.

[16] Sean R Eddy. What is a hidden Markov model? *Nature Publishing Group*, 22:1315–1316, 2004.

[17] C Eggeling, S Berger, L Brand, J R Fries, J Schaffer, A Volkmer, and C A M Seidel. Data registration and selective single-molecule analysis using multiparameter fluorescence detection. *Journal of Biotechnology*, 86:163–180, 2001.

[18] John Safwat Eid. *Two-photon Dual Channel Fluctuation Correlation Spectroscopy: Theory and Application.* PhD in Biophysics and Computational Biology, University of Illinois at Urbana-Champaign, 2002.

[19] Th. Förster. Transfer mechanisms of electronic excitation. *Discussions of the Faraday Society*, 27:7–17, 1959.

[20] H C Gerritsen, A Draaijer, D J van den Heuvel, and A V Agronskaia. *Handbook of Biological Confocal Microscopy, Third Edition*, pages 516–534. Springer, 2006.

[21] D M Grant, D S Elson, D Schimpf, C Dunsby J Requejo-Isidro, E Auksorius, I Munro, M A Neil, P M French, E Nye, G Stamp, and P Courtney. Optically sectioned fluorescence lifetime imaging using a Nipkow disk microscope and a tunable ultrafast continuum excitation source. *Opt Lett*, 30(24):3353–3355, 2005.

[22] E Gratton and M Limkeman. A continuously variable frequency cross-correlation phase fluorometer with picosecond resolution. *Biophys J*, 44(3):315–324, 1983.

[23] Phyllis I Hanson and Howard Schulman. Neuronal Ca^{2+}/calmodulin-dependent protein kinases. *Annu. Rev. Biochem.*, 61:559–601, 1992.

[24] David M Jameson, Enrico Gratton, and Robert D Hall. The measurement and analysis of heterogeneous emissions of multifrequency phase and modulation fluorometry. *Applied Spectroscopy Reviews*, 20:55–106, 1984.

[25] Joseph M Johnson, Taekjip Ha, Steve Chu, and Steven G Boxer. Early steps of supported bilayer formation probed by single vesicle fluorescence assays. *Biophys J*, 83:3371–3379, 2002.

[26] Sally A Kim, Katrin G Heinze, M Neal Waxham, and Petra Schwille. Intracellular calmodulin availability accessed with two-photon cross-correlation. *PNAS*, 101(1):105–110, 2004.

[27] Joseph R Lakowicz and Aleksander Balter. Theory of phase-modulation fluorescence spectroscopy for excited-state processes. *Biophysical Chemistry*, 16:99–115, 1982.

[28] Valeria Levi, QiaoQiao Ruan, and Enrico Gratton. 3-D particle tracking in a two-photon microscope: Application to the study of molecular dynamics in cells. *Biophysical Journal*, 88:2919–2928, 2005.

[29] Anders Malmendal, Sara Linse, Johan Evanäs, Sture Forsén, and Torbjörn Drakenberg. Battle for the EF-hands: Magnesium-calcium interference in calmodulin. *Biochemistry*, 38:11844–11850, 1999.

[30] M Margittai, J Widengren, E Schweinberger, G F Schröder, S Felekyan, E Haustein, M König, D Fasshauer, H Grubmüller, R Jahn, and C A M Seidel. Single-molecule fluorescence resonance energy transfer reveals a dynamic equilibrium between closed and open conformations of syntaxin 1. *PNAS*, 100(26):15516–15521, 2003.

[31] L D Mayer, M J Hope, and P R Cullis. Vesicles of variable sizes produced by a rapid extrusion procedure. *Biochim et Biophy Acta*, 858:161–168, 1986.

[32] Sean A McKinney, Chirlmin Joo, and Taekjip Ha. Analysis of single-molecule FRET trajectories using hidden Markov modeling. *Biophysical Journal*, 91:1941–1951, 2006.

[33] X Michalet, O H W Siegmund, J V Vallerga, P Jelinsky, J E Millaud, and S Weiss. Photon-counting H33D detector for biological fluorescence imaging. *Nuclear Instruments and Methods in Physics Research A*, 576:133–136, 2006.

[34] Burak Okumus, Timothy J Wilson, David M J Lilley, and Taekjip Ha. Vesicle encapsulation studies reveal that single molecule ribozyme heterogeneities are intrinsic. *Biophysical Journal*, 87:2798–2806, 2004.

[35] Hye Yoon Park, Sally A Kim, Jonas Korlach, Elizabeth Rhoades, Lisa W Kwok, Warren R Zipfel, M Neal Waxham, Watt W Webb, and Lois Pollack. Conformational changes of calmodulin upon Ca^{2+} binding studied with a microfluidic mixer. *PNAS*, 105:542–547, 2008.

[36] S Pelet, MJ Previte, L H Laiho, and P T So. A fast global fitting algorithm for fluorescence lifetime imaging microscopy based on image segmentation. *Biophys J*, 87(4):2807–2817, 2004.

[37] G I Redford and R M Clegg. Polar plot representation for frequency-domain analysis of fluorescence lifetimes. *J Fluoresc*, 15(5):805–815, 2005.

[38] Hugo Sanabria, Michelle Digman, Enrico Gratton, and M Neal Waxham. Spatial diffusivity and availability of intracellular calmodulin. *Unpublished preprint*, 2008.

[39] Gunnar F. Schröder and Helmut Grubmüller. Maximum likelihood trajectories from single molecule fluorescence resonance energy transfer experiments. *Journal of Chemical Physics*, 119:9920–9924, 2003.

[40] Julia M Shifman, Mee H Choi, Stefan Mihalas, Stephen L Mayo, and Mary B Kennedy. Ca^{2+} calmodulin-dependent protein kinase II (CaMKII) is activated by calmodulin with two bound calciums. *PNAS*, 103(38):13968–13973, 2006.

[41] Brian D Slaughter, Jay R Unruh, Michael W Allen, Ramona J Bieber Urbauer, and Carey K Johnson. Conformational substates of calmodulin revealed by single-pair fluorescence resonance energy transfer: Influence of solution conditions and oxidative modification. *Biochemistry*, 4:3694–3707, 2005.

[42] R D Spencer and G Weber. Measurements of subnanosecond fluorescence lifetimes with a cross-correlation phase fluorometer. *Annals New York Academy of Sciences*, 158:361–376, 1969.

[43] Anita Teleman, Torbjörn Drakenberg, and Sture Forsen. Kinetics of Ca^{2+} binding to calmodulin and its tryptic fragments studied by ^{43}Ca-NMR. *Biochim et Biophys Acta*, 873:204–213, 1986.

[44] E B van Munster, J Goedhart, G J Kremers, E M Manders, and T W Gadella Jr. Combination of a spinning disc confocal unit with frequency-domain fluorescence lifetime imaging microscopy. *Cytometry A*, 71(4):207–214, 2007.

[45] M Neal Waxham, Ah-lim Tsai, and John A Putkey. A mechanism for calmodulin (CaM) trapping by CaM-kinase II defined by a family of CaM-binding peptides. *Journal of Biological Chemistry*, 273(28):17579–17584, 1998.

[46] Yihong Yao, Christian Schöneich, and Thomas C Squier. Resolution of structural changes associated with calcium activation of calmodulin using frequency domain fluorescence spectroscopy. *Biochemistry*, 33:7797–7810, 1994.

Author's Biography

Ryan Anthony Colyer was born in Pennsylvania on February 9, 1980. During college he held internships at Cigital and Los Alamos National Laboratory. He graduated from Allegheny College in 2002 with a double major in physics and computer science, and a minor in psychology. He then enrolled in the University of Illinois at Urbana-Champaign, where he obtained a Master of Science in Physics in 2004. In 2006, he moved to the University of California - Irvine, where he completed his doctoral research while remaining enrolled as a student at the University of Illinois. Following the completion of his Ph.D. in 2008, Colyer will begin a position as a post-doctoral scholar in the Department of Chemistry and Biochemistry at the University of California - Los Angeles in Dr. Shimon Weiss's laboratory.